Stony Brook University

The official electronic file of this thesis or dissertation is maintained by the University Libraries on behalf of The Graduate School at Stony Brook University.

Evaluation of 4H Silicon Carbide and Gallium Nitride Crystals for Power Electronics &

Lighting Applications

A Thesis Presented

by

Xiaolin Yang

to

The Graduate School

in Partial Fulfillment of the

Requirements

for the Degree of

Master of Science

in

Materials Science and Engineering

Stony Brook University

May 2016

Stony Brook University

The Graduate School

Xiaolin Yang

We, the thesis committee for the above candidate for the

Master of Science degree, hereby recommend

acceptance of this thesis.

Michael Dudley – Thesis Advisor
Professor, Department of Materials Science and Engineering

Balaji Raghothamachar – Second Reader
Research Professor, Department of Materials Science and Engineering

T.A. Venkatesh – Third Reader
Associate Professor, Department of Materials Science and Engineering

This thesis is accepted by the Graduate School

Charles Taber
Dean of the Graduate School

Abstract of the Thesis

Evaluation of 4H Silicon Carbide and Gallium Nitride Crystals for Power

Electronics & Lighting Applications

by

Xiaolin Yang

Master of Science

in

Materials Science and Engineering

Stony Brook University

2016

Silicon carbide is a promising semiconductor material with more preferable properties than the traditional materials like silicon dioxide and gallium arsenide. With large band-gap, high breakdown voltage, high thermal conductivity and good resistance in radiation environment, SiC is widely used in electronic devices especially under high frequency, high voltage and high temperature. Despite of its good properties, the application of SiC is limited by the growth of high quality single crystal boule, namely, the defects inside the SiC crystals have deleterious effects on the performance of devices made of it. In this thesis, the combination of techniques including Synchrotron White Beam X-ray Topography, Monochromatic X-ray Topography and Nomarski Optical Microscopy is used, and the distribution of dislocations including Basal Plane Dislocations, Threading Edge Dislocations and Threading Screw Dislocations are measured and other defects like Stacking Fault, Low Angle Grain Boundary and V-shape are also characterized.

Due to the wide band-gap and high efficiency of emitting light, gallium nitride is widely used in LED industry. Similar with silicon carbide, gallium nitride crystal also suffers from the defects inside the crystals. In this thesis, High Resolution of X-ray Diffraction is used to measure the rocking curve of the crystal, and software HXRD is used to simulated the rocking curve of perfect crystal. And the Full Width Half Maximum is calculated to evaluate the overall quality of the crystal.

Table of Contents

List of Figures

List of Tables

List of Abbreviation

SiC   Silicon Carbide

GaN   Gallium Nitride

SWBXT   Synchrotron White Beam X-ray Topography

HRXRD   High Resolution X-ray Diffraction

CVD   Chemical Vapor Deposition

LED   Light Emitting Diode

MOSFET   Metal-Oxide-Semiconductor Field-Effect Transistor

BPD   Basal Plane Dislocation

TED   Threading Edge Dislocation

TSD   Threading Screw Dislocation

TMD   Threading Mixed Dislocation

PD   Partial Dislocation

PPD   Prismatic Plane Dislocation

SF   Stacking Fault

MP   Micropipe

LAGB   Low Angle Grain Boundary

SEM   Scanning Electron Microscope

FWHM   Full Width Half Maximum

List of Symbols

N_D	Doping Concentration
D_{sf}	Distance between sample and film
D_{ss}	Distance between source and sample
R_s	Resolution of XRT technique
d_{hkl}	Interplanar spacing of (hkl) plane
θ_B	Bragg angle
λ	Wavelength
μ	Linear absorption
F_{hkl}	Structure factor
ρ	Dislocation density

Acknowledgement

First I would like to give my deep and sincere gratitude to Prof. Michael Dudley, my advisor, for providing me this opportunity to work in the field of semiconductor materials characterization. I really appreciated his guidance not only on the research work but also on life and future.

Second I would like to thank Prof. Balaji Raghothamachar for his patient guidance during research. His encouragements and suggestions help me overcome the difficulties in the experiment.

I would like to thank my parents for supporting me finishing my master degree financially and psychologically, providing me the opportunity getting such an exciting and unforgettable experience in Stony Brook University. Without them, all the accomplishments are impossible.

I would like to thank Prof. T.A. Venkatesh for being the reviewer of my master's thesis.

I would like to thank my colleagues, Dr. Yu Yang, Dr. Jianqiu Guo, Dr. Ouloide Goue, for all their helps during my research.

Technique support: Beamline 1-BM at the Advanced Photon Source (APS) at Argonne National Laboratory (ANL).

Chapter 1. Introduction of SiC

1.1 Structure of SiC

Silicon Carbide is a compound semiconductor material made of silicon atoms and carbon atoms, both of which have four valence electrons, and each atom is bound to four of the other kind of atoms, to make a tetrahedron as shown in Fig 1.1. SiC has approximately 200 polytypes, which are only different in [0001] direction. For close-packed layers of (0001) plane, there are three possible stacking positions, as indicated in Fig 1.2.
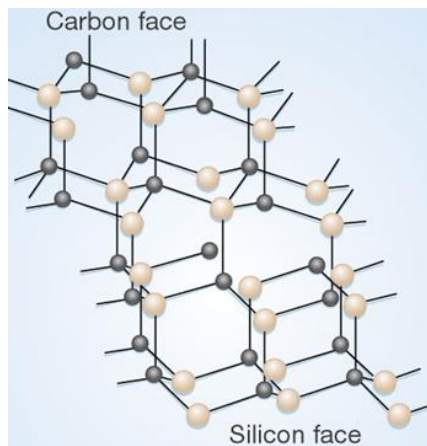
Fig1.1 Ball and stick Model of Silicon Carbide. Yellow ball stands for silicon atom, and Black ball is carbon atom.
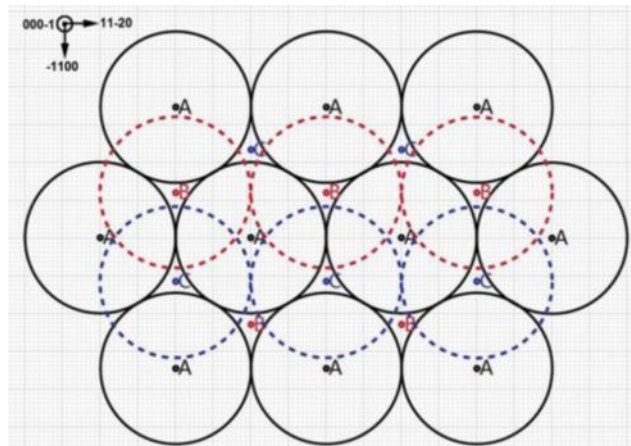
Fig1.2 Three stacking positions in [0001] direction, labeled by A, B, and C respectively.

If the plane (0001) stacks in sequence ABCABCABC…..the whole structure is called 3C-SiC, a FCC lattice structure with three layers periodical unit. Similarly, if the (0001) plane stacks in the sequence ABA'C'AB…..we name it 4H-SiC, which means each layer of atoms is hexagonal close-packed, and 4 layers of them make a periodical unit. Here A' is the same position with A, but with a rotation of the tetrahedron through 180 degrees, which will be discussed later. Another common polytype of SiC is 6H-SiC, whose stacking sequence is ABCB'A'C'ABC….. meaning 6 layers of atoms is a periodical unit and each layer is hexagonal close-packed. Now we see the crystal in the direction of $[11\bar{2}0]$, and we can have the projection on plane $(11\bar{2}0)$ to explain the twinned position indicated by A', B' or C'. One single tetrahedron is shown in Fig 1.3
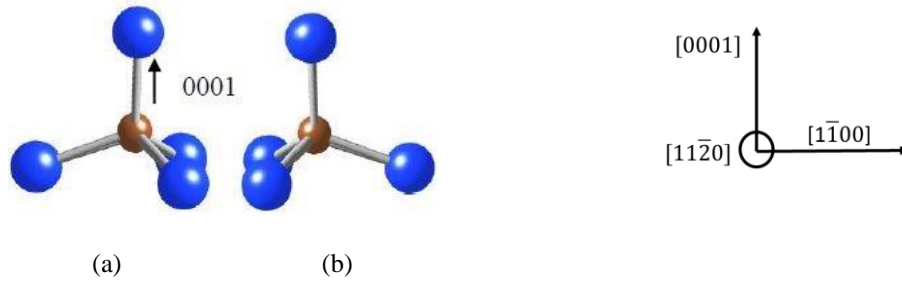
Fig 1.3 The original tetrahedron of SiC(left) and twinned

tetrahedron(right) on $(11\bar{2}0)$ projection.

From Fig 1.3 we could know that, those two tetrahedrons are basically the same, the only difference is that the short double bond is on the right side in tetrahedron (a), while it's in the opposite direction in tetrahedron (b). It seems like (b) is obtained by rotating 180 degree of (a). Thus we label them with A and A' to indicate the slight difference between them. Fig 1.4 shows the $(11\bar{2}0)$ projection of several common polytypes of SiC, which are ABCABC…for 3C-SiC, ABA'C'AB…for 4H-SiC and ABCB'A'C'…for 6H-SiC.
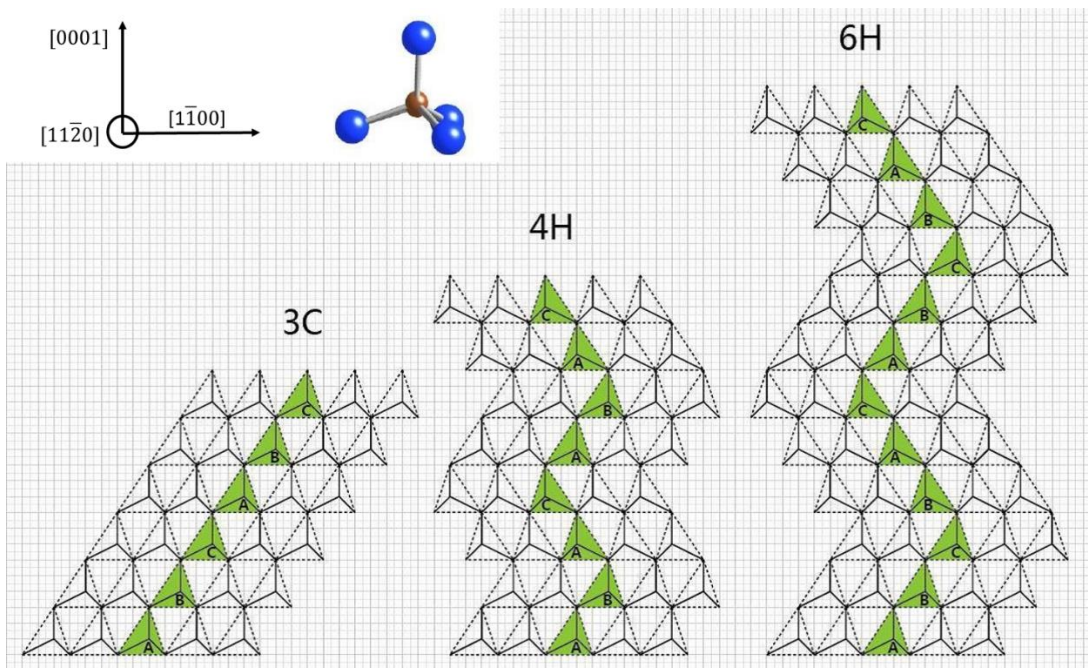
Fig 1.4 $(11\bar{2}0)$ projection of 3C-SiC, 4H-SiC and 6H-SiC[1]

1.2 Properties and Applications of SiC

SiC is a wide band-gap semiconductor with properties superior to than Silicon and GaAs for power devices. The details of its properties are listed in Table 1.1 [2].

Table 1.1 Comparison of Semiconductor Material Properties

	Si	GaAs	SiC(4H)	GaN
Saturation Electron Drift Velocity(10^7cm/s)	1.0	1.2	2	2.5
e-mobility at $N_D=10^{16}$ cm^{-3}(cm^2/v•s)	1200	6500	//(0001): 60 ⊥(0001): 400	900
Band-Gap(eV)	1.1	1.42	3.2	3.4
Breakdown Field at $N_D=10^{17}$ cm^{-3}(MVcm^{-1})	0.6	0.6	//(0001): 3.0 ⊥(0001): 2.5	2-3

Usually, Si-based semiconductors fail above 200˚C [1], because of the leakage current of PN junction at reverse bias is high enough. However, when it comes to wide band-gap semiconductors like SiC, operating temperatures can be extended to 600˚C [3], since it now needs much more energy, which means higher temperature, to activate the intrinsic electrons to the conduction band to form the leakage of current. Similarly, wide band-gap semiconductors also have a higher breakdown electric field than Si-based semiconductors, due to the higher energy it needs to get intrinsic carrier flow. At the point of breakdown, the outside reverse bias can accelerate extrinsic carriers, free electrons and holes, which can provide energy for activating intrinsic carrier, and this makes the leakage current grow significantly.

Another advantage SiC has over Si-based semiconductor is that SiC possesses a high thermal conductivity K, which is 3.7 Wcm^{-1}K^{-1}, compared with 1.5 Wcm^{-1}K^{-1} for Si [4]and 0.55 Wcm^{-1}K^{-1} for GaAs [5]. This means SiC is stable at high temperature without degradation, which is important in fabrication of power devices, and the packing density can also be higher due to the good thermal property. Other than the high breakdown voltage and high thermal conductivity, SiC also possesses good resistance in a radiation environment, high hardness and good mechanical and chemical stability, all of which make SiC a promising material for use in various industrial applications[6][7][8][9][10], as abrasives and cutting tools, structural materials, power electronic device and LEDS.

1.3 Defect Structure of 4H-SiC

There are several kinds of defects which exist in silicon carbide crystals, like dislocations, stacking faults, and 3C-SiC polytype inclusion. For dislocations, basically we have two types, the growth dislocations and the deformation-induced dislocations. They are different in formation mechanism and hence in configurations.

Growth Dislocations

Growth dislocations are formed during the growth of the crystal, by replicating the dislocations that thread the moving growth front. These threading dislocations can originate from dislocations that already exist in the seed, or from the relaxation of stress because of damage on the seed surface, and also can be originated from the release of stress due to some impurity and doping atoms. Since growth dislocations thread the moving of growth front, they always run along the normal of growth front, which is perpendicular to the growth plane. That means the dislocation line is parallel to the growth direction, and based on Burger's vector, growth dislocations can be classified into 3 kinds, Threading Edge Dislocation (TED), Threading Screw Dislocations (TSD), and Threading Mixed Dislocation (TMD). TED indicates that dislocation line is along growth direction, which is (0001) in SiC, and the Burger's vector is equal to $\frac{1}{3}[11\bar{2}0]$, that is perpendicular to the line direction. TSD means the Burger's vector is parallel to line direction which is [0001]. TMD is the mixture of TSD and TED, so the angle between Burger's vector and dislocation line is between 0 degree and 90 degrees.

Deformation-Induced Dislocations

Deformation-induced dislocations are always related to the slip systems (hkl)<uvw>, critical resolved shear stress and the original dislocations, where (hkl) is the index of slip plane and <uvw> is the index of slip direction. The original dislocations could be growth dislocations, dislocation loops around impurities, surface dislocation loops associated with surface damage and point defects [1]. Stress usually comes from several aspects, like the thermal stress due to inhomogeneous heating of the substrate during CVD crystal growth, from different thermal expansion between substrate and epilayer, and also could come from the lattice mismatch of substrate and epilayer. If the stress is larger than the critical resolved shear stress, it will activate the dislocation multiplication and increase the dislocation density significantly. Since deformation-induced dislocations are from the slip and multiplication of the original dislocations, it always looks like loops bowing out from fixed points, sometimes are half loops and concentric loops. Common deformation-induced dislocations are BPDs, which lie on the basal plane (0001), and the Burger's vector is $\frac{1}{3}[11\bar{2}0]$. Since the basal plane is the most close-packed plane in the lattice of 4H-SiC, it is the primary slip plane for dislocations. And $[11\bar{2}0]$ is the close-packed direction with atoms lie in the shortest distance with each other, so it is the primary slip direction. Hence slip system (0001)< $11\bar{2}0>$ is the primary slip system for 4H-SiC, and dislocations slip and multiply on

(0001), which is called basal plane.

1.3.1   Fundamental Information of Defects in SiC

A schematic diagram of BPD, TSD and TED are shown in Fig1.5 [11].
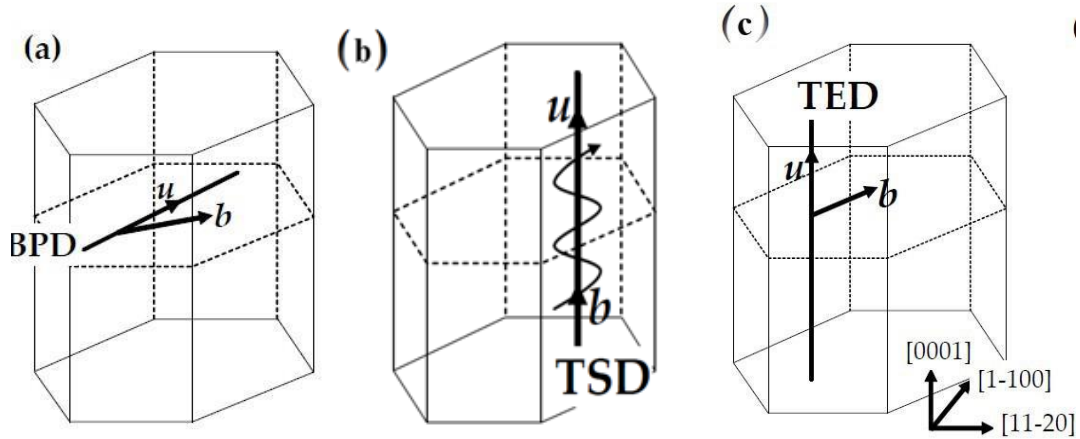
Fig 1.5 (a) A BPD lines in (0001) plane; (b) A TSD with line direction [0001] and burger's vector is parallel to
dislocation line also in [0001]; (c) A TED with line direction along [0001] and burger's vector in basal plane.

Other than the dislocations described above, in 4H-SiC, there are also some major
defects existing, such as Shockley type stacking faults (SFs), Frank-type SFs and low
angle grain boundaries (LAGBs) which are composed of TEDs or BPDs and Micro-
Pipes (MP) (or superscrew dislocations) [11]. All the parameters for these several major
defects are listed in Table 1.2.

Table 1.2 Parameters of different defects in 4H-SiC

	Dislocation line (u)	Burger's vector (b)
BPD	// (0001) plane	1/ 3<11-20> (3.08 Å)
TED	Roughly // [0001] direction	1/ 3<11-20> (3.08 Å)
TSD	// [0001] direction	nc (10.05nÅ) n(integer) ⩽2, or c+a
MP	// [0001] direction	nc (10.05nÅ) n(interger)>2
Shockley PD	// (0001) plane	1/3<1-100> (1.778Å)
Frank PD	// (0001) plane	1/2c, 1/4c

1.3.2   Defect Formation and Influences

As described earlier, SiC is a promising material for power devices because it possesses
many favorable properties which are characteristic of its crystal structure. But the
widespread application of SiC power device is mainly limited by the defects introduced
during crystal growth and device fabrication. For example, if the substrate we use has
some TEDs and TSDs in it, then when the crystal grows, these threading dislocations
will be replicated and propagate, as investigated by F. Wu[12]. And the aggregation of

TEDs can also form Low Angle Grain Boundaries (LAGB) and become pinning points for BPDs gliding, as discussed in M. Dudley, Y. Chen, and X. Huang's research [13]. Some inclusions on the surface of the substrate will result in the formation of Micropipes, which are fatal defects in electronic devices [14]. Micropipes have hollow-core structures with diameters from 0.1-10μm [15]. They can reduce the breakdown voltage of a PN diode by more than 50% [14], which we need to avoid. Another defect that forms during crystal growth is a polytype inclusion. For example, 3C-SiC inclusion in 4H-SiC, which has been investigated by M. Dudley[16], and this formation of polytype will bring lattice mismatch between the matrix and itself, and the mismatch will lead to a strain field around them, which could provide the force for dislocation multiplication. Similarly, if we don't heat the substrate homogenously during the deposition of the epilayer, there will be thermal stresses generated [17], especially in the thin epilayer and induce dislocation multiplication, generating more BPDs, which could also lead to the nucleation of stacking faults.

Chapter 2. Characterization Techniques of SiC Crystal

To characterize single-crystal semiconductor materials, several techniques are used, such as Synchrotron X-ray Topography and Nomarski Microscopy, which will be introduced in the following sections.

2.1 Fundamentals of X-ray Diffraction

Synchrotron X-ray Topography and High Resolution X-ray Diffraction are based on the basic principle of X-ray diffraction. Since X-rays are electromagnetic waves, when the beam hits any material, the wave interacts with the electrons inside the material, then the wave after interaction is called scattered beam. When the incident beam goes through crystal and is diffracted by the atom arranged in the crystal lattice, the scattered beams by each atoms will interact with each other, producing a diffracted beam. There are two kinds of theory related to the diffraction process, one is kinematic diffraction theory and the other is dynamic diffraction. Kinematic diffraction is the commonest considered theory, which ignores the multiple scattering inside the crystal and is a good approximation of imperfect crystal, thin perfect crystal and powder. When we talk about perfect crystals, the loss of intensity in re-scattering should be taken into account. As shown in Fig 2.1, the x-ray beam get diffracted by a plane of atoms, the phase of it changes by $\pi/2$, so when the crystal is perfect enough to let the diffracted beam get a secondary diffraction, the phase of the beam will change by another $\pi/2$, which means it is out of the phase with the incident beam and the diffracted intensity will decrease by this secondary diffraction. This effect is called primary extinction, which is the basis of dynamic theory.
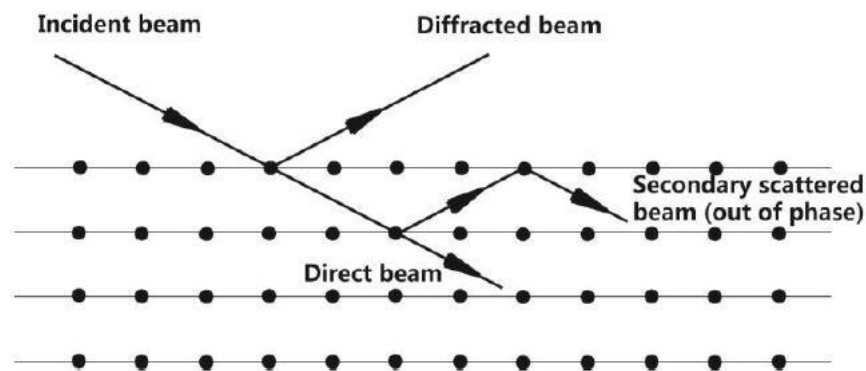
Fig 2.1 Simplified diagram for explanation of dynamic theory

2.2 Synchrotron X-ray Topography

X-ray Topography (XRT) is a nondestructive technique enabling one to 'see' the defects inside crystals, especially on semiconductor materials like Silicon Carbide (SiC), Gallium Nitride (GaN), Silicon (Si), and Sapphire (Al_2O_3). XRT images recorded from crystals with dislocation density less than $10^6 \, cm^{-2}$ enable dislocations to be seen clearly.

It is a powerful tool for crystal grower to monitor and evaluate the growth quality and provide instruction for improving the growth conditions.

2.2.1 History of XRT

The development of XRT is shown in Table 2.1, which lists all the stages on XRT from the discovery of X-ray to the application of different types of Synchrotron XRT.

Table 2.1 Different stages of the development of XRT [24]

Year	Name	Achievement
1895	Wilhelm Rontgen	The discovery of X-rays
1931	Berg	Recorded first Monochromatic x-rays diffraction pattern on rock salt using laboratory source
1945	Barrett	Report results from single crystals of silicon ferrite with improved contrast
1945	Wooster	The establish of 'topography' in literature
1949	Guinnier and Tennevin	Using polychromatic x-ray in transmission from lab x-ray sources on aluminum samples
1957	Lang	Section topography
1974	Tuomi *et al.*	First synchrotron radiation topography on Silicon samples
1975	Hart	'Synchrotron' White beam x-ray topography (SWBXT)
1977	Tanner	'Synchrotron' Monochromatic X-ray Topography (SMBXT)

2.2.2 Introduction of Synchrotron XRT

The XRT Technique is improved significantly by the development of the Synchrotron X-ray Source. Synchrotron X-ray Radiation is generated by electrons accelerated to near the speed of light. First, the Electron beam is accelerated by ultrahigh voltage in the Booster Ring, then the electrons are moved to the Storage Ring, where they can keep their speed with the help of magnetic field. And at the tangent direction of the storage ring, there will be x-rays emitted, which are called synchrotron x-rays as schematically shown in Fig 2.2. Synchrotron X-rays have a wide spectrum with the range from 0.2Å--2Å, so we call it white beam synchrotron X-ray. If we want to use monochromatic beam, a monochromator is placed in the path of the white beam before the sample. Monochromators are usually highly perfect crystals with specific plane as

the diffracting surface, and there're basically two kinds, single channel cut and asymmetric channels, both of which are shown in Fig 2.3. Other advantages that synchrotron X-ray has are less divergent angle, high flux, and high brilliance, all of which make synchrotron X-ray widely used for X-ray topography and other X-fay techniques for studying materials.
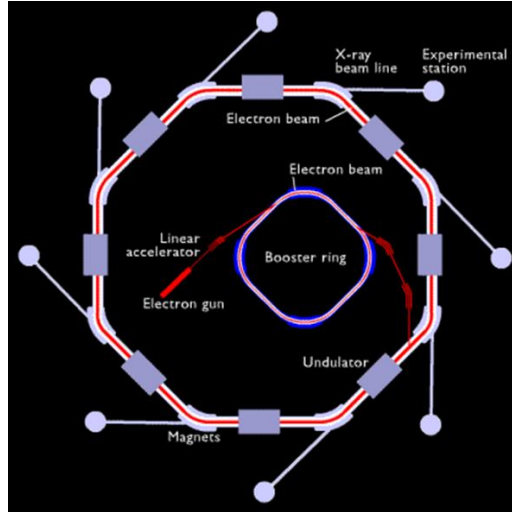

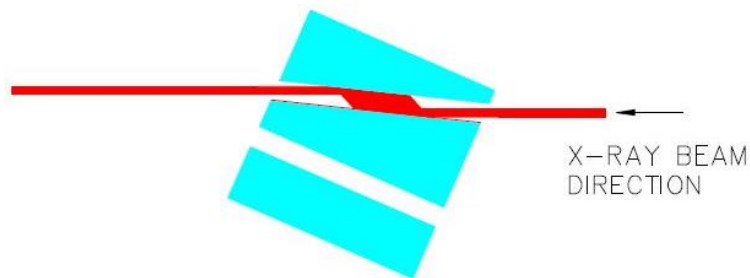Fig 2.2 Schematic diagram for Synchrotron X-ray Source

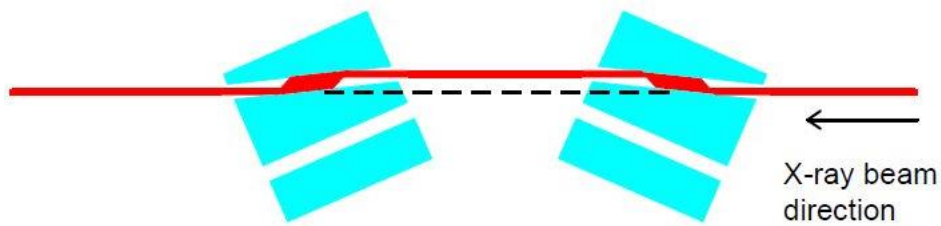Fig 2.3 (a) Schematic diagram of single channel monochromator

Fig 2.3 (b) Schematic diagram of asymmetric channel monochromator

The resolution of XRT technique is decided by the following equation

$$R_s = D_{sf} \frac{S}{D_{ss}}$$

Where D_{sf} is the distance between sample and film, D_{ss} is source-sample distance, and

S is the size of incident beam. The beam we use at the Advanced Photo Source in Argonne National Laboratory 1-BM is up to 10 cm width and 1cm height at 90 m from source. And from the equation above, we can see a small size beam, combined with a large sample-source distance can make a high resolution of XRT Technique.

2.2.3 Imaging Geometry

When we talk about X-ray diffraction in a bulk crystal, we say the diffraction beam comes from the diffraction of a set of planes. And all the diffraction from different sets of planes obey Bragg's Law, which is indicated by the following equation:

$$2d_{hkl} \sin \theta_B = \lambda$$

Where d_{hkl} is the spacing between two (hkl) planes, λ is the wavelength of incident X-ray, and $\sin \theta_B$ is the angle between incident beam and plane (hkl), which is same with angle between reflection beam and plane (hkl). It is called Bragg Angle, and each set of planes has its own Bragg Angle. Since we use white beam source, literally, when the beam hit the sample in front of it, every set of (hkl) plane with certain incident angle θ_B could find a correspondent wavelength λ to get diffracted beam. But in real experiment, we might miss patterns of some sets of planes because of the intensity is too low.

In Synchrotron Whitebeam X-ray Topography (SWBXT) experiment, sample is placed at the path of incident beam, and the recording film is put either behind or in the front of the sample to get exposure when there're reflected beams from the crystal. There are basically three kinds of geometry of SWBXT, which are transmission geometry, back-reflection geometry and grazing geometry.

(1) Transmission Geometry

In transmission geometry, the film is placed behind the sample to record the diffracted beam from the crystal. The simplified diagram for transmission SWBXT is shown in Fig 2.4, and the diffracted pattern that is simulated with Program LauePt [18] is shown in Fig 2.5, while Fig 2.6 shows the real film that record the diffracted pattern after exposure, developing and fixing.
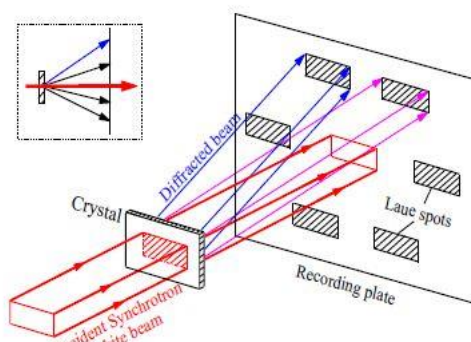
Fig 2.4 Simplified diagram for transmission geometry
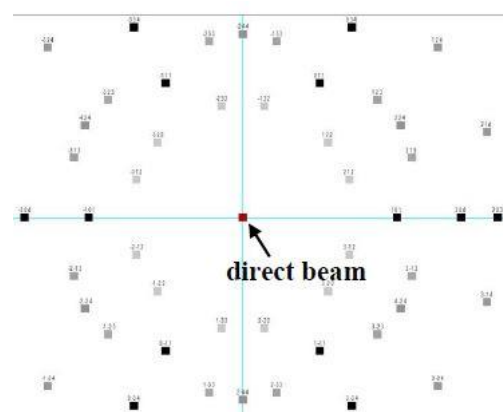
Fig 2.5 Simulated diffracted pattern from SiC with surface plane (0001) and side plane (11-20), by LauePt program

Usually for a 4 inch or 6 inch SiC wafer, we do not record every diffraction spot on the pattern. Selected diffraction spots with low indices like (11-20) and (1-100) are recorded. Fig 2.6 shows the image of a 4 inch SiC wafer from (1-210) diffraction pattern and the magnified image of part of the wafer.
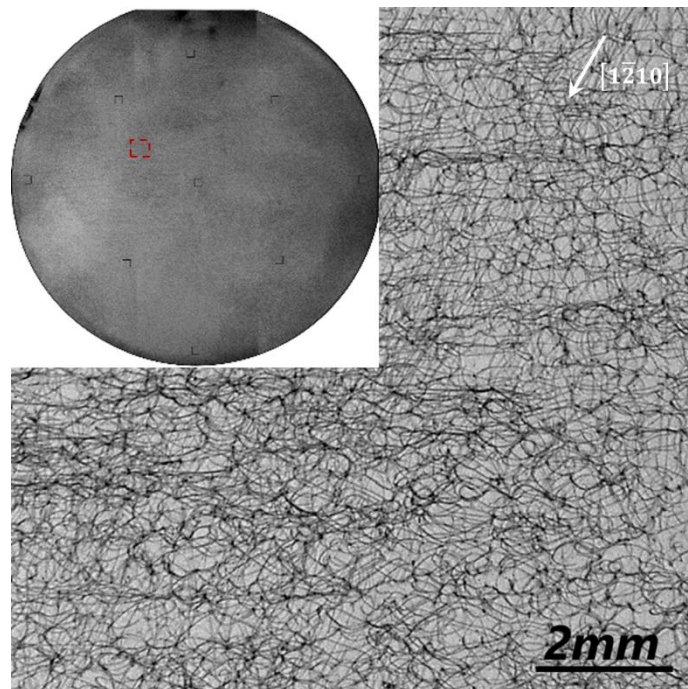
Fig 2.6 Transmission geometry SWXRT image of SiC on (1-210) diffraction

From Fig 2.6 we can see the main part is magnified from part of the whole sample which is indicated by a red rectangle. There're many black lines twist and tangle with each other, these black lines are Basal Plane Dislocations (BPDs).

Transmission Geometry is usually used on bulk crystals and wafers. The high intensity of synchrotron source make it possible for the beam to go through the entire sample thickness, so images can reveal all the information of the sample, both from substrate and epilayer. And for the samples that are bigger than the beam, which means we cannot cover the entire sample with one shot, we usually separate the whole sample into several parts, and we do a scan mode, take several shots, and combine the images together to get the information from the whole sample.

(2) Back-Reflection Geometry

Another important geometry is back-reflection geometry. From the name we could guess that diffracted beam is reflected back, which is the opposite direction with incident beam. The schematic diagram for back reflection geometry is shown in Fig 2.7 and Fig 2.8 is the simulated reflected pattern with LauePt program.
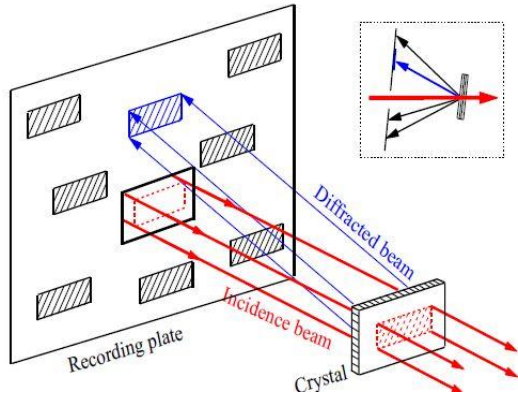
Fig 2.7 Back-Reflection Geometry of SWXRT
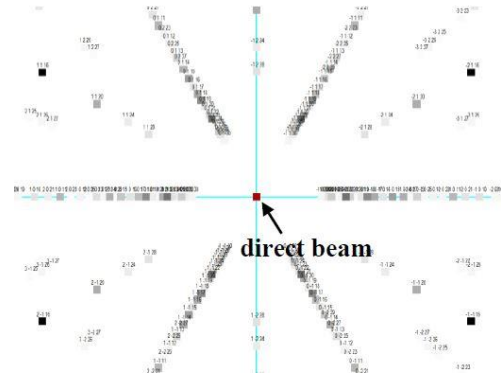
Fig 2.8 Simulated pattern for SiC with surface (0001)
and side plane (11-20)

From Fig 2.7 we can clearly see that along the beam path, there are source, film and sample successively. X-ray doesn't go through the whole sample, probably because the materials has a high absorption factor for x-ray or because the sample is too thick for x-ray to penetrate. The beam exits from the same surface as the one it enters without hitting any deep part of the sample, so back-reflection geometry XRT is a good way to characterize the property of surface materials, like the epitaxy layer.

An image of SiC with (00012) diffraction using back-reflection geometry is shown in Fig 2.9, and from the picture we can see some very small white dots, which are TEDs, and some white circles with dark ring surrounding it are TSDs. The radius of the dots and circles are positively proportional to the Burger's vector. As we talked in the last chapter, Burger's vector of TED is $1/3<11\text{-}20>$, which is about 3.08Å in SiC, while the smallest Burger's vector of TSD is $<0001>$, which is about 10.05Å. So the radius of TSD is much larger than TED.

Fig 2.9 Back-reflection image of SiC with g=00012 diffraction [11]

(3) Grazing Geometry

The last geometry that is usually used is grazing geometry, which means the angle between incident beam and surface of the sample is very small, it is nearly parallel to the surface, and the diffracted beam exits the surface in a very large angle nearly 90 degree. With a very small incident angle, the same beam can cover larger area of the sample, and the penetration depth is less than that for back-reflection. The grazing geometry is shown in Fig 2.10 and the image taken with this geometry is shown in Fig 2.11.

Fig 2.10 Grazing geometry of SWXRT   Fig 2.11 Grazing geometry image of SiC with (11-28)
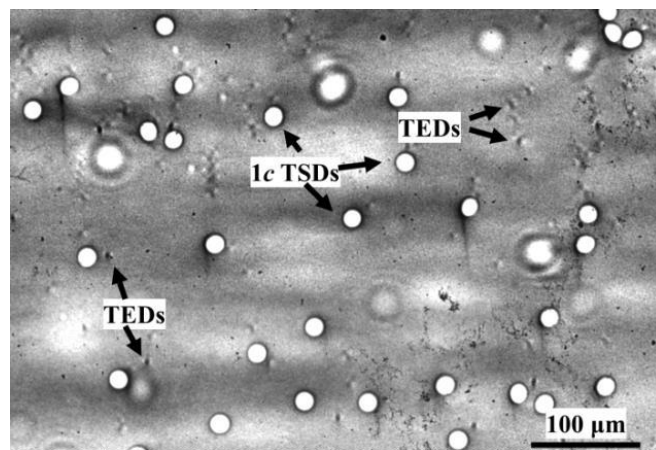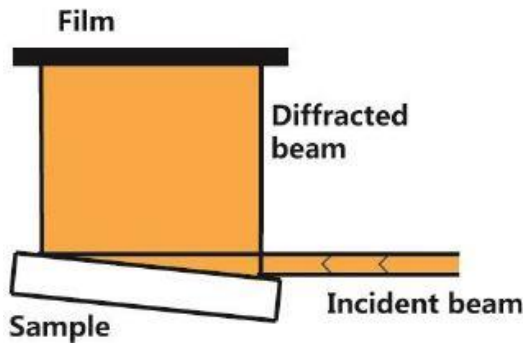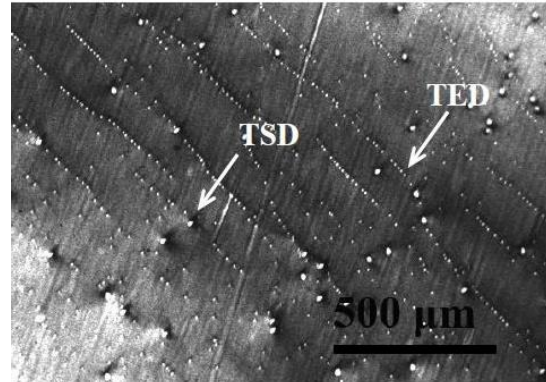
diffraction [11]

Grazing Geometry is very sensitive to the surface and since we can choose different grazing angle (the angle between incident beam and surface), penetration depth can vary from several hundred nanometers to dozens of microns. Hence it is a good tool to create a depth profile of defects for the crystal [1]. Fig 2.11 is image from (11-28) diffraction, whose Bragg's Angle is about 45.2 degree, and the penetration depth is about 30 microns. In grazing geometry, TSD is not a circle any more, it becomes to oval shape, and TED is similar, but with a smaller size, which are studied by F. Wu[19].

2.2.4 Image Contrast

In the films shown above, we could always see some white or dark contrast within the grey background. The grey background comes from the diffraction of matrix, that is, the perfect crystal. As we talked about at the beginning of this chapter, for perfect crystal, x-ray have dynamic diffraction, and the phenomenon of primary extinction leads to lower intensity, which makes the image grey. While the white and dark contrast comes from the diffraction of defects, either strengthen the intensity or reduce the intensity. There're two kinds of contrast formation mechanism in SWBXT, orientation contrast and extinction contrast.

(1) Orientation Contrast

Orientation contrast happens because of the sudden orientation change of grain boundaries with the matrix perfect crystal. According to Bragg's Law, for the same set of atom planes, they have the same Bragg angle under a specific wavelength λ, which means the diffracted beam exit from the surface of sample in the same direction.

However, the existence of some defects, like grain boundaries, changes the orientation of its surrounding part abruptly, then the incident angle is not the same, so the atoms in vicinity of a dislocation must choose another wavelength λ_1 to match this new incident angle θ_1, in order to follow the Bragg's Law. θ_1 is definitely different from Bragg Angle θ_B of the perfect part, so diffracted angle is also not the same with the perfect part, which means the diffracted beam exits in different diffraction. Then some beam will superimpose with others in one side, resulting in high intensity of x-ray and a dark contrast in the image. Contradictorily, on the other side of the dislocation, some beam will be separated with others, resulting in low intensity of x-ray and a white contrast in the image. The schematic illustration of this geometric analysis is shown in Fig 2.12, and a real film is shown in Fig 2.13 to verify the analysis.
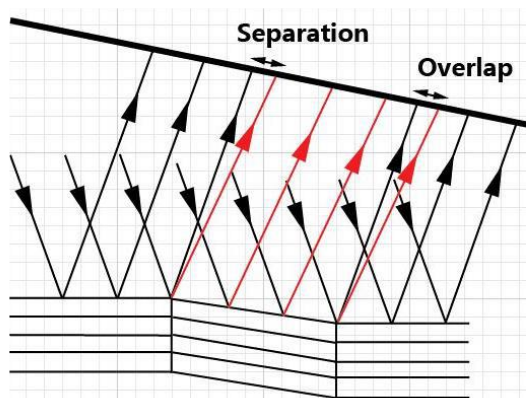

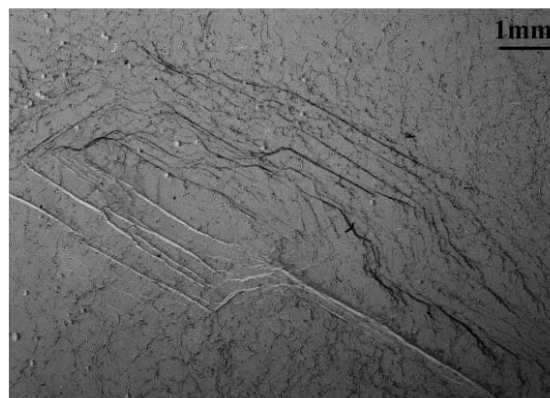Fig 2.12 Schematic diagram for orientation contrast   Fig 2.13 Grazing SWXRT on (11-28) diffraction to
show white and dark contrast [1]

From Fig 2.13, we can see clearly that on one side of the sub-grain, the contrast is white while on the other side of the sub-grain, the contrast is dark. This is correspondent the separation part and the overlap part of the schematic diagram.

(2) Extinction Contrast

Extinction contrast consist of three components: direct image, dynamic image and intermediate image. The dominant condition for each component is based on a parameter $\mu \cdot t$, where μ is the absorption coefficient, and t is the thickness of the crystal. When $\mu t < 1$, meaning in a low absorption condition, direction image gives the dominant contrast. When $\mu t > 4$, meaning in a high absorption condition, dynamic image gives the dominant contrast. If $1 < \mu t < 4$, the contrast mainly comes from intermediate image.

As we know, when x-ray is diffracted by a crystal, it follows the Bragg's Law, which gives a specific angle θ_B for a certain set of atom plane (hkl), and under a certain wavelength λ. It seems like only θ_B could satisfy the Bragg Equation, which is

$$2d_{hkl} \sin \theta_B = \lambda$$

But the fact is that in dynamic diffraction, x-ray beam can be diffracted within a narrow range around Bragg Angle, and the range is known as Rocking Curve with the width

Δθ. The width of rocking curve is very small, usually around a few seconds of arc, which is much less than the divergent angle of x-ray beam, though synchrotron source has a less divergent angle than normal x-ray source. So only a small part of the incident beam could be diffracted. However, if there're some defects inside the crystal, like dislocations, changing the lattice orientation, it will allow the other part of the x-ray beam, whose divergent angle is outside of the rocking curve, to get diffracted. And since the influence area of these defects are limited, so there's no primary extinction for the diffraction. The higher portion of x-ray beam that could be diffracted and no primary extinction, make the intensity of diffracted beam from the area of defects higher, leading to a dark contrast in the film. Some details about the rocking curve, absorption coefficient and Bragg angle is shown in Table 2.2[1].

Table 2.2 Parameters in SWBXT of 4H-SiC

hkil	d_{hkl}(Å)	θ_B	λ (Å)	μ(mm^{-1})	F_{hkl}	$\Delta\theta$
0004	2.51	6˚	0.52	0.5	40.8	2.66"
11-20	1.54	10˚	0.53	0.6	41.2	1.69"
1-100	2.67	8˚	0.74	1.6	13.48	1.42"
1-101	2.58	7˚	0.62	1	19.98	1.66"
11-28	0.97	37.2˚	1.17	6.4	18.46	1.31"
d_{hkl}--interplanar distance; θ_B--Bragg angles; λ--wavelength; μ--linear absorption coefficient; F_{hkl}--structure factor; $\Delta\theta$--rocking curve width						

2.3 Normaski Optical Microscopy

In the laboratory, there's another tool to see the defects in the SiC wafer, which is Normaski Optical Microscopy with Nikon Polarizing Microscope Eclipse E600W POL embedded. This microscopy has a resolution of nearly 0.1 micron, and could be used to observe as-grown surface, the samples' surface morphology and defect feature and the etch pits pattern of etched 4H-SiC wafers [11]. The polarized light function that equipped in this microscope can help to enhance the contrast of defects and have a good quality of the image.

Chapter 3. Defect Study of 4H-SiC Substrate and Epilayer

3.1 Introduction

In this chapter, three 4H-SiC wafer samples are analyzed in detail. Two are substrates and the third is substrate with homo-epilayer grown on Si-face. With the help of transmission geometry SWBXT, grazing geometry monochromatic x-ray topography and Nomarski Optical Microscopy, defects like Basal Plane Dislocation, Prismatic Dislocation, Threading Screw Dislocation, Threading Edge Dislocation, Stacking Fault, and V-shape defect are observed and analyzed.

3.2 Experiment

Synchrotron x-ray topography experiment is done at Advanced Photon Source, Argonne National Laboratory. For White Beam X-ray, the Beam size we use is 43mm x1mm, and for monochromatic Beam, the beam size is 10cm x 5mm. The picture of the wafer is shown in Fig 3.1. It has an off-cut angle of 4˚, that is, the surface is 4˚ with respect to the basal plane, which is (0001) along the [11-20] direction. There are two flats on the edge of the wafer to determine the orientation. The major flat is perpendicular to direction [1-100], and the minor flat is perpendicular to [11-20] direction. With the major flat at the top, and the minor flat to the right, the top surface is the silicon face. When doing transmission XRT, usually we put silicon face as the exit face for the beam, because defects from the exit face of the sample has better contrast in X-ray diffraction experiment. And silicon face is more important because normally we grow epilayer on that face. Since the beam size is not big enough to cover the whole wafer, we separate it into three parts, left, middle and right part. For each part, we scan it from bottom to top and get the entire image of the wafer. During the analysis of image, dislocation density need to be calculated. For the density of BPD and Prismatic Plane Dislocation (PPD), cm^{-2} is used as the unit. A 2mm x 2mm square is taken, and the total length of BPD and PPD, L within this square is measured with Program Spot. Then the thickness of this wafer t is measured with the micrometer gauge. So the dislocation density ρ is calculated by the following equation:

$$\rho = \frac{L}{S \bullet t}$$

Where S stands for the area of the square, which is 4 cm^2 here.

For density of Threading Dislocation, we also take a 2cm*2cm square, and count the number of threading dislocation in this square N, then the density of threading dislocation is calculated as

$$\rho = \frac{N}{S}$$

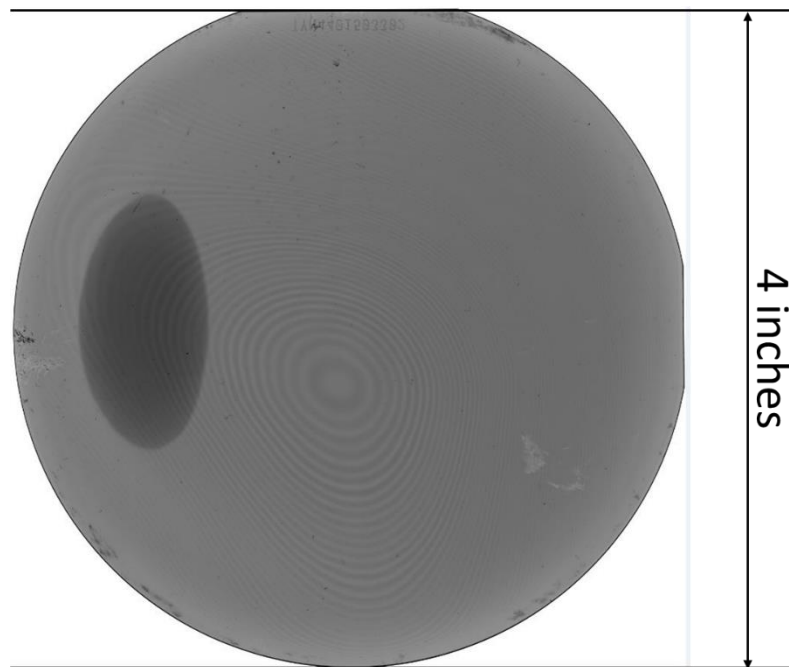Where S is the area of the square, which is 4 cm^2

Fig 3.1 Image of 4-inch SiC wafer

For one wafer, we choose 9 squares in different position of the sample, and calculated the density of BPD (PPD) dislocation and threading dislocation respectively for 9 squares, then take the average value of these 9 squares.

3.3 Results and Discussion

Sample 1-- CN4N01502318

(1) Transmission Geometry White Beam XRT

Transmission geometry XRT image is shown in Fig 3.2. The diffraction vector is $\vec{g} = [\overline{1}\overline{1}20]$, and the thickness of this wafer is 359 μm. Those 9 squares chosen in the wafer are indicated by black outline in the image, and the magnified images show the BPD (PPD) distribution of each square in Fig 3.3.
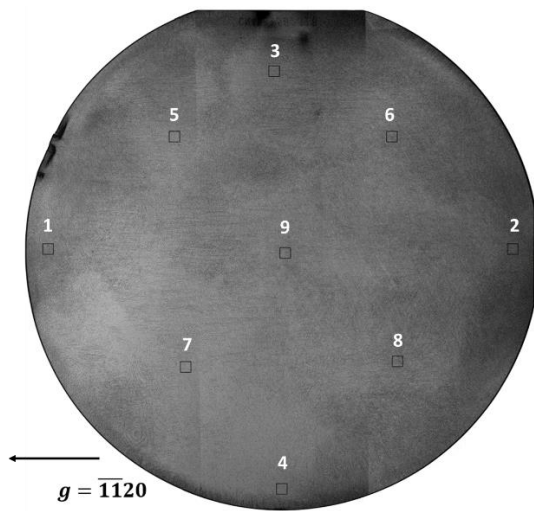

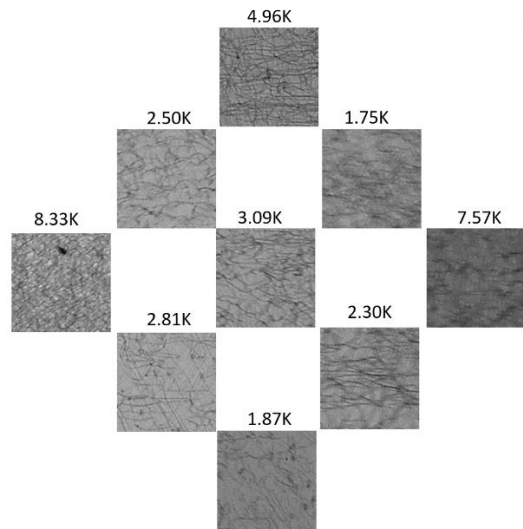Fig 3.2 Transmission geometry image with diffraction vector [-1-120]

Fig 3.3 Magnified image of transmission geometry for 9 different squares (unit for the density is cm^{-2})

Using the method we talked about in chapter 3.2, the density of BPD (PPD) in 9 squares is calculated as shown in Table 3.1

Table 3.1 The distribution of BPD density of sample 1

Region	1	2	3	4	5	6	7	8	9
Density (10^3cm^{-2})	8.33	7.57	4.96	1.87	2.5	1.75	2.81	2.3	3.09

The average value is 3.91 x 10^3 cm^{-2}. We could see that the density of dislocation at the edge of the wafer is higher than it in center. The reason is that during the growth of the crystal, there's a stress concentration at the edge of the boule due to inhomogeneous heating and boule fixing. So when the stress is larger than the critical resolved shear stress on the basal plane, BPDs will begin to glide and multiply. BPDs glide from edge to center, so the density on the edge is larger than it in the center. For BPDs, stress on the basal plane could activate them to glide, while for Prismatic Dislocations, stress on the prismatic plane could make them glide. This stress may come from the vertical thermal gradient along the growth direction of the boule. And those black lines parallel

to each other, which are approximately 60° oblique to [$\overline{1}1\overline{2}0$] direction, are prismatic dislocations.

Other than BPD (PPD), we also found some Low Angle Grain Boundary (LAGB) at the edge of the wafer, which is indicated by a red rectangle and shown in Fig 3.4. And the magnified image is shown in Fig 3.5.
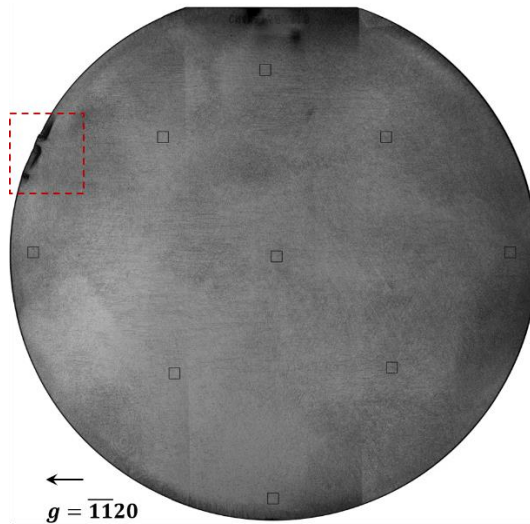

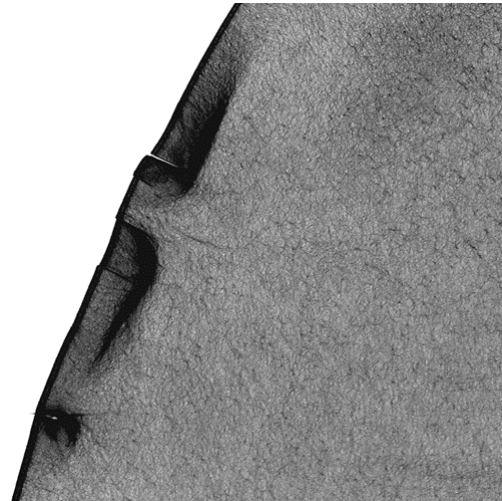Fig 3.4 Image of LAGB by transmission geometry XRT

Fig 3.5 The magnified image of LAGB indicated by the red rectangle in Fig 3.4

From Fig 3.5 we can see many dislocations aggregated around the bold black line, which is the LAGB. This indicates the formation mechanism of LAGB. LAGB is made of arrays of TEDs. These threading dislocations are always barriers to glide of BPDs, so when TEDs aggregate in an array, it prevent BPDs gliding further and make BPDs accumulated around the TED array. The schematic diagram is shown in Fig 3.6.
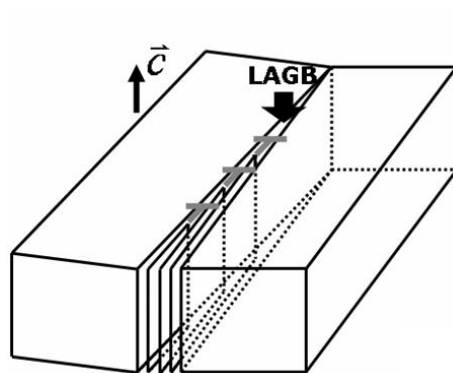

Fig 3.6 Schematic diagram of the formation of LAGB

(2) Grazing Geometry Monochromatic Synchrotron XRT

When doing grazing geometry XRT experiment, we use monochromatic x-ray, which come from white beam synchrotron x-ray, and just use a monochromator we talked about early, before it hit the sample. The energy of the beam we use is 8.99k eV, diffraction vector is [-1-128], and the Bragg angle is 45.2˚. In [-1-128] diffraction, we can observe TEDs, TSDs, TMDs and MPs. Since the incident beam has a very little angle with the surface of the sample, it cannot go through the whole sample and the penetration depth is about 40 microns, which means all the defects we see in this image is within 40 microns depth from the surface. Similar with transmission geometry, in grazing geometry, the beam size cannot cover the whole wafer, so we separate it into two parts, and scan each part separately then combine them together. Step size we choose is 0.015˚, and usually three or four contours can cover the whole length of the sample. The grazing geometry image is shown in Fig 3.7. Since images from grazing geometry XRT are very sensitive to surface defect or bending, we can see from Fig 3.7 that the contrast of some part of the sample is white or not dark enough. The reason is that because of bending on the surface, the incident angle of planes in these white region is out of the rocking curve angle range $\triangle\theta$, and they're not able to diffract the x-ray beam. We name these regions as unoptimized regions, which don't provide us with all the information from the sample, so we rotate the sample a little bit, that is change the incident angle a little bit to let planes in umoptimized region diffract the beam. Then we overlap these two images to get a full display of the sample quality with every part of optimized region.
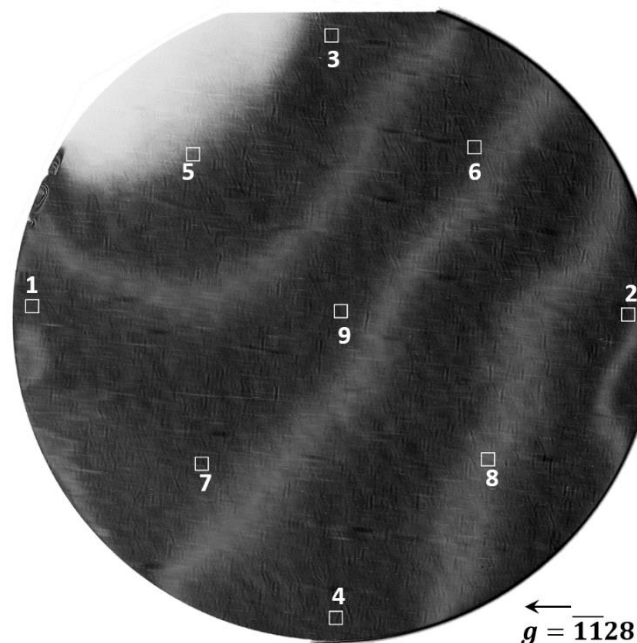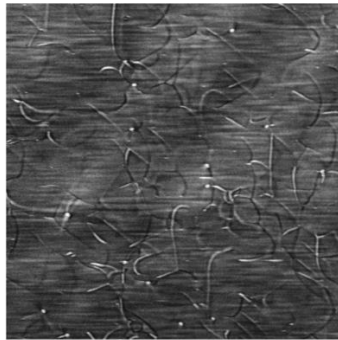

Fig 3.7 Grazing geometry image of [-1-128]diffraction

We also choose 9 different positions, which is square with dimension 2mm*2mm, in the wafer to measure the density of TEDs and TSDs respectively, then calculate the

average value of it. The magnified images for these 9 positions is shown in Fig3.8—Fig3.17, and the density is also shown in the figure.
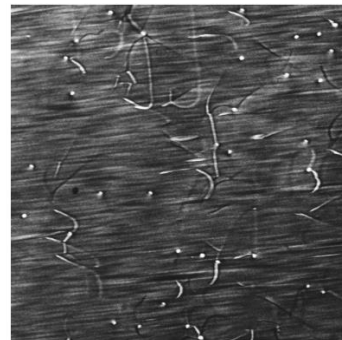

#1   TSD : 400 cm^{-2} ; TED : 875 cm^{-2}

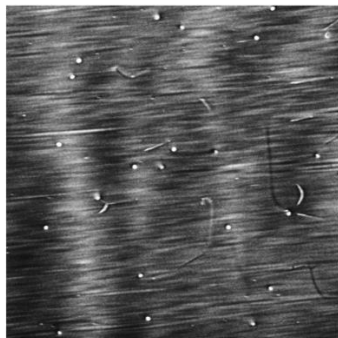Fig 3.8 Position #1 magnified image with TED and TSD density
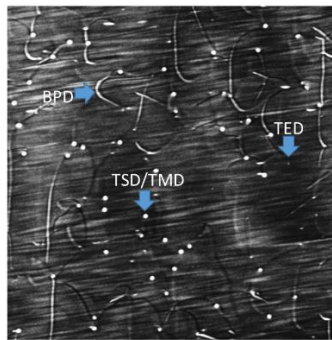
#2 TSD : 1325 cm^{-2} ; TED : 800 cm^{-2}

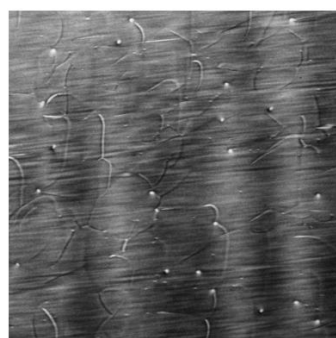Fig 3.9 Position #2 magnified image with TED and TSD density

#3   TSD : 800 cm^{-2} ; TED : 150 cm^{-2}
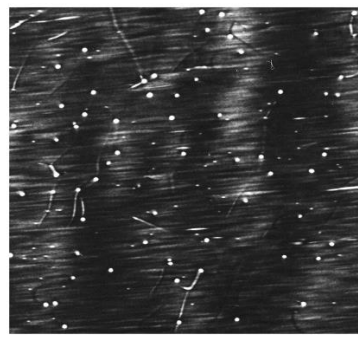
Fig 3.20 Position #3 magnified image with TED and TSD density

#4   TSD : 550 cm^{-2} ; TED : 900 cm^{-2}

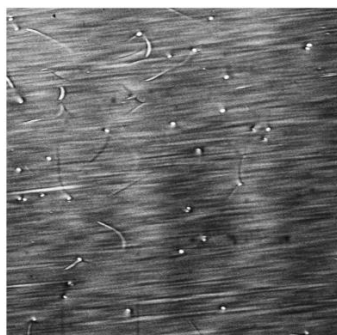Fig 3.11 Position #4 magnified image with TED and TSD density

#5 TSD : 550 cm^{-2} ; TED : 1800 cm^{-2}

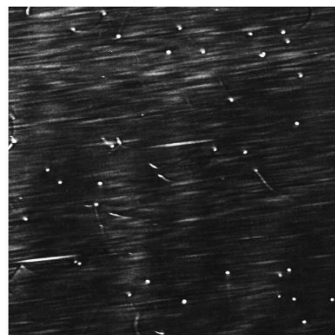Fig 3.12 Position #5 magnified image with TED and TSD density

#6   TSD : 1600 cm^{-2} ; TED : 1825 cm^{-2}

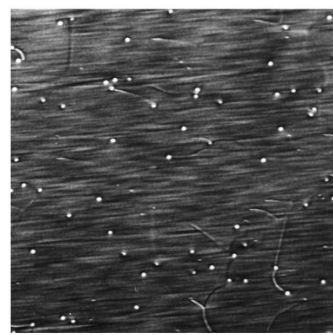Fig 3.13 Position #6 magnified image with TED and TSD density

#7 TSD : 900 cm^{-2} ; TED : 250 cm^{-2}

Fig 3.14 Position #7 magnified image with TED and TSD density

#8 TSD : 950 cm^{-2} ; TED : 275 cm^{-2}

Fig 3.15 Position #8 magnified image with TED and TSD density

#9 TSD : 1475 cm^{-2} ; TED : 600 cm^{-2}

Fig 3.16 Position #9 magnified image with TED and TSD density

For the whole wafer, we use the average value of these 9 positions to evaluate dislocation density. The distribution of TED and TSD is shown in Table 3.2.

Table 3.2 Distribution of TEDs and TSDs in Sample 1

Region	1	2	3	4	5	6	7	8	9
TSD Density (cm^{-2})	400	1325	800	550	550	1600	900	950	1475
TED Density (cm^{-2})	875	800	150	900	1800	1825	250	275	600

The image with distribution of density of TED and TSD is shown in Fig 3.17. The average density of TED in this sample is 830.6 cm^{-2}, and the average density of TSD is 950 cm^{-2}.
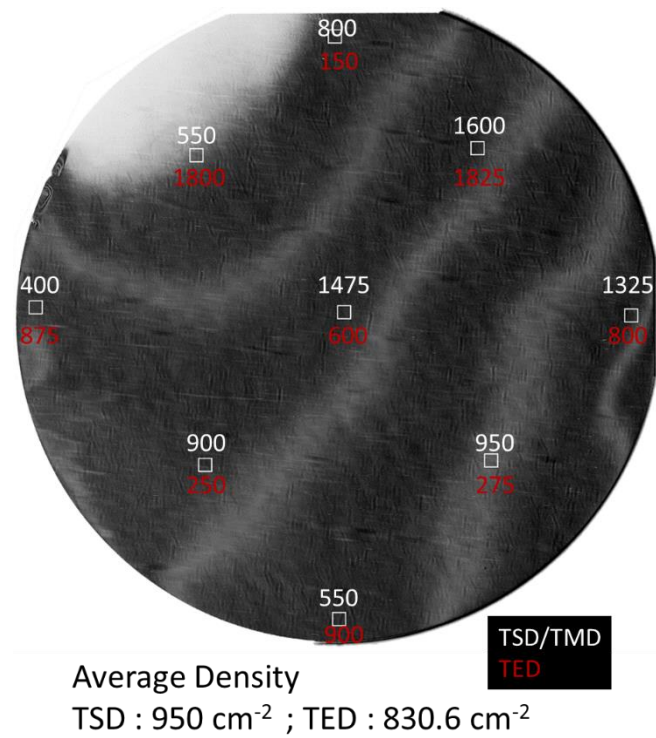

Fig 3.17 The distribution of density of TED and TSD/TMD in the whole wafer

In this grazing geometry image, other than TED, TSD and TMD, we also find some miropipes which are shown in Fig 3.18. The position that micropipes locate is indicate with red dot.
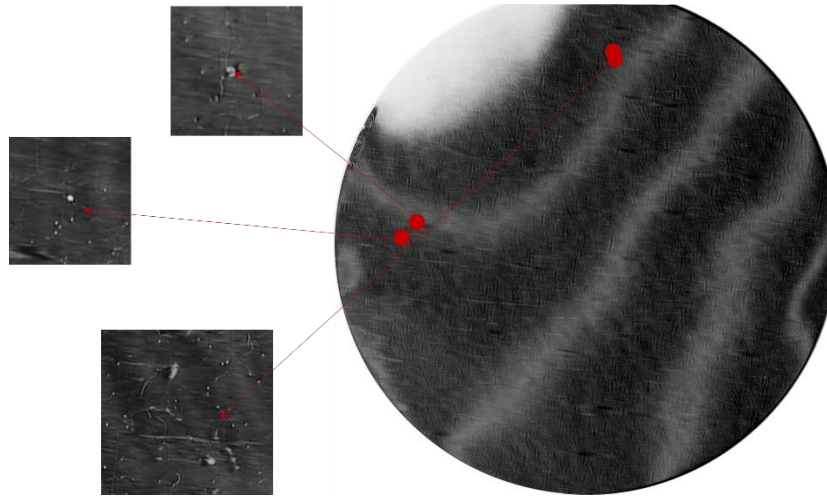
Fig 3.18 The distribution of Micropipe in grazing geometry image

Sample 2-- CN4N01502612

(1) Transmission Geometry White Beam Synchrotron XRT

Sample 2 is also a 4 inch SiC substrate. With the same method we use to characterize the first sample, we also measure the BPD distribution in transmission geometry image shown in Fig 3.19 and Fig 3.20.
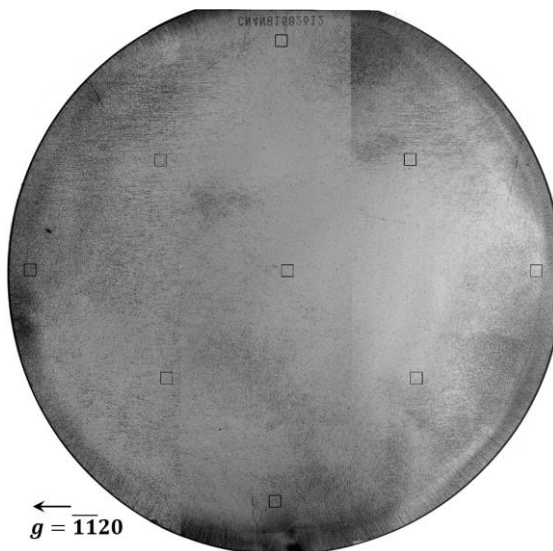

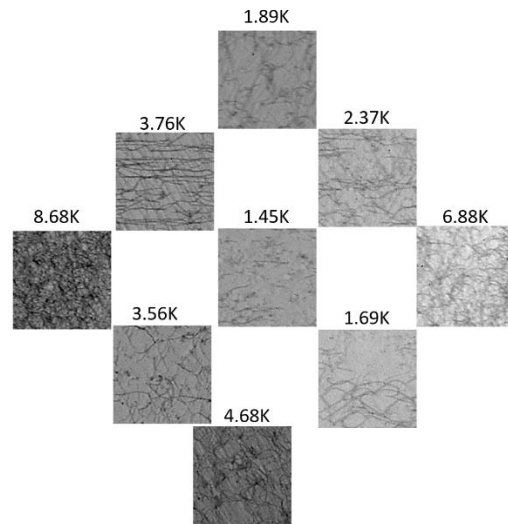Fig 3.19 Transmission geometry image with diffraction vector [-1-120]

Fig 3.20 Distribution of density of BPD in transmission geometry image

The thickness of sample 2 is 370 μm, and the average density of BPD is 3.88 x 10^3 cm^{-2}. The BPD density in selected regions is shown in Table 3.3.

Table 3.3 The distribution of BPD density of sample 2

Region	1	2	3	4	5	6	7	8	9
Density ($10^3 cm^{-2}$)	8.68	6.88	1.89	4.68	3.76	2.37	3.56	1.69	1.45

Besides these 9 square positions chosen to measure the BPD density, we notice that there's a region has a very low density at a little bit right of the center. Then we also magnify that part to calculate the BPD density. The region is indicated by a red rectangle in Fig 3.21, and magnified picture of that part is shown in Fig 3.22.
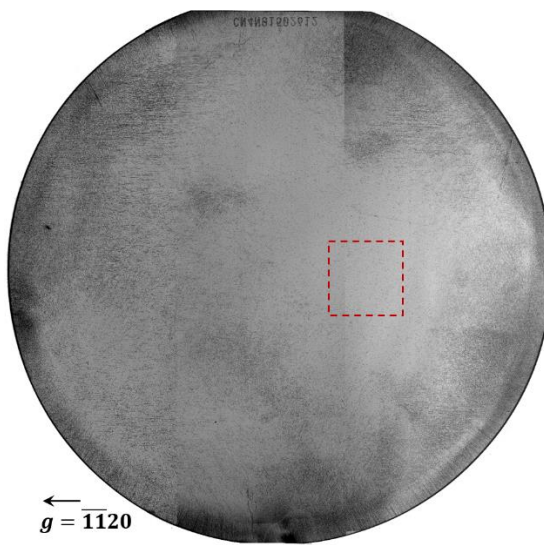

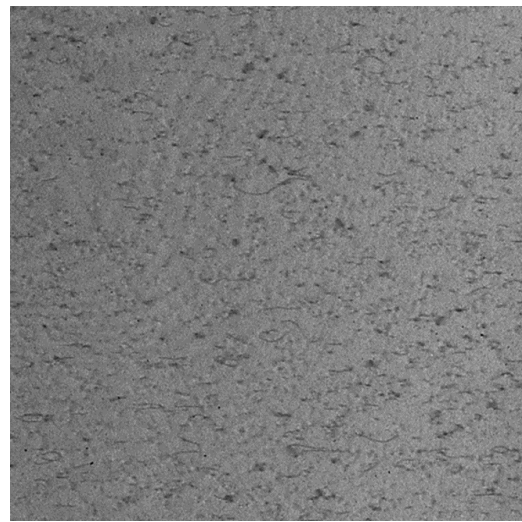Fig 3.21 selected part with low BPD density

Fig 3.22 Magnified picture of selected part with low BPD density

From Fig 3.22 we could barely see long black lines tangling with each other, but just very few single lines, which means the density of BPD is very low. The black dots in the picture are threading dislocations, which can only be seen in very low BPD density region. The area of this selected region is 1cm x 1cm, the BPD density measured is 340.1 cm^{-2}, about only 10% of the other region.

In this film image, we also find other defects like micropipe, which is shown in Fig 3.23
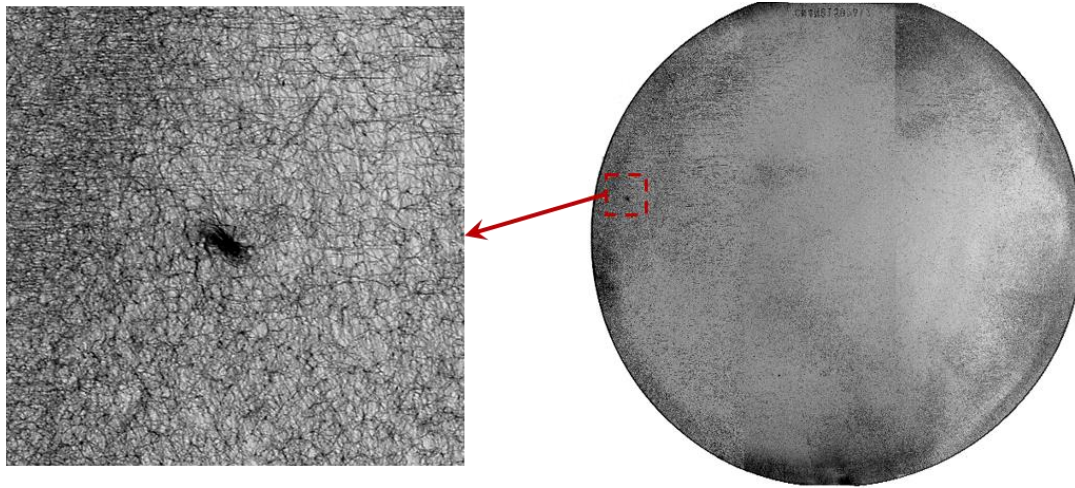
Fig 3.23 A micropipe found in transmission image and its magnified figure.

From Fig 3.23 we could see that micropipe is the big black dot surrounded by bunch of BPD, because micropipe is the center of stress concentration.

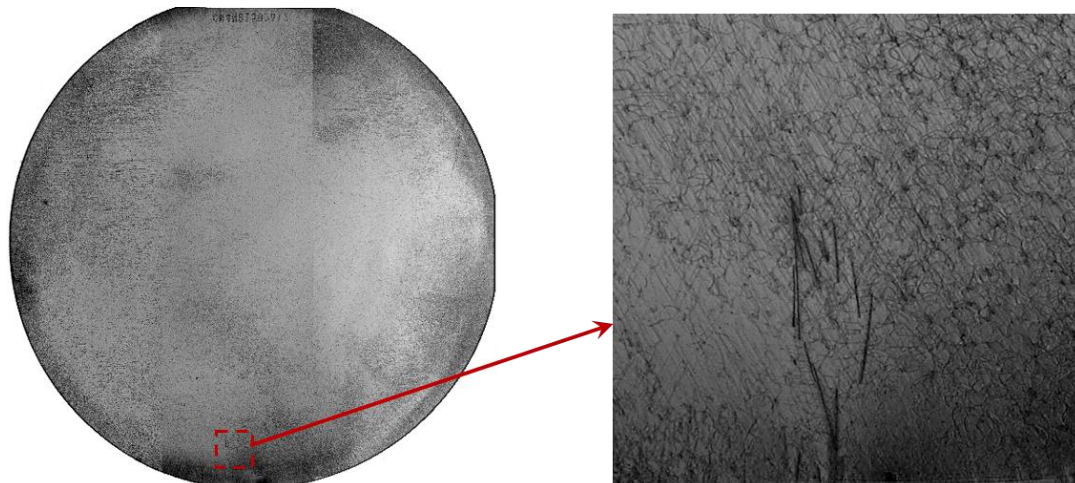Another defect we find in this sample is deflected TSD/TMD, which is shown in Fig 3.24.

Fig 3.24 Deflected TSD/TMD found in transmission image and its magnified image

At the edge of the wafer, there're some bold black lines. They are TSD/TMD that reflect on the basal plane. Since the burger's vector of threading dislocation is bigger than it of basal plane dislocations, the width of the line is larger than BPDs. And these deflected TSD/TMD could form stacking fault during the growth of the crystal.

(2) Grazing Geometry Monochromatic Synchrotron XRT

With the same method we did in the experiment for the first sample, we also using monochromatic x-ray in grazing geometry to detect TED, TSD/TMD and other defects like Micropipes. The 9 positions selected is indicated in Fig 3.25, and the distribution of TED and TSD in each region is shown in Fig 3.26—Fig 3.34. The area of selected

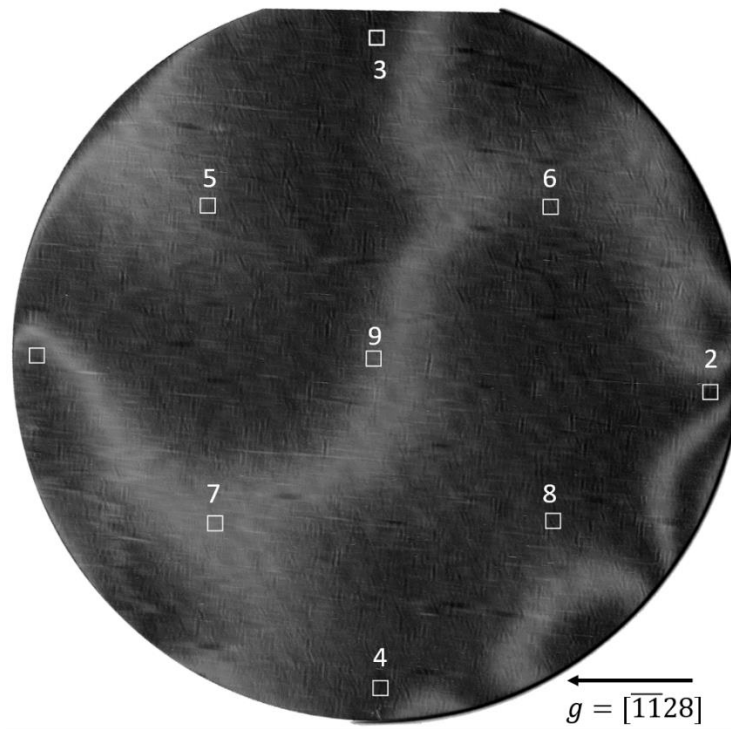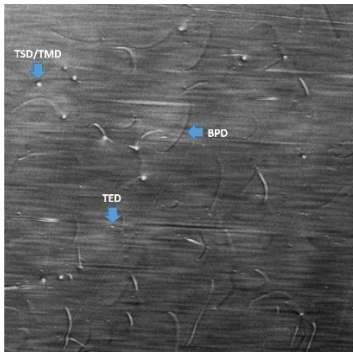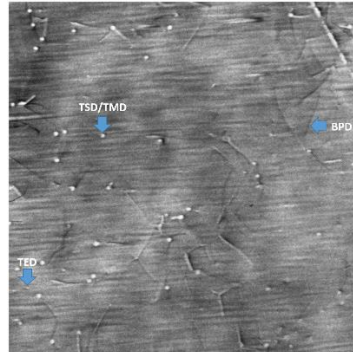region is 2mm x 2mm and the sample thickness is 370 μm.

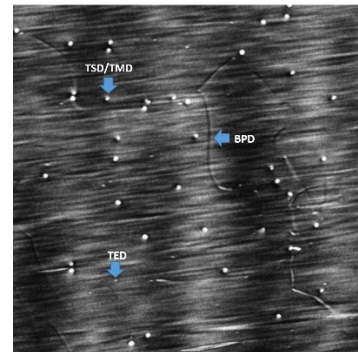Fig 3.25 Grazing geometry image with 9 selected positions indicated with square and number

TED:1700cm^{-2}; TSD:325cm^{-2}

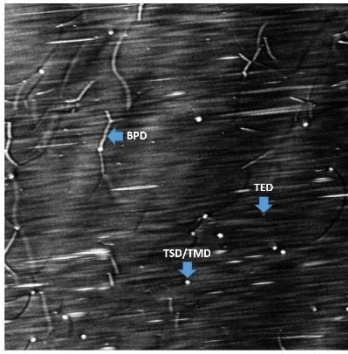Fig 3.26 Magnified image for region #1

TED:375cm^{-2}; TSD:875cm^{-2}
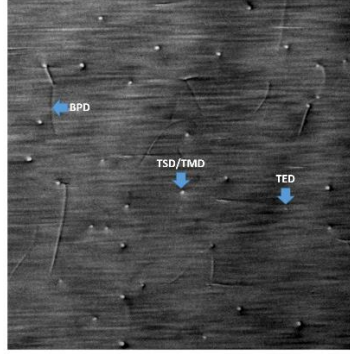
Fig 3.27 Magnified image for region #2

TED:725cm^{-2}; TSD:1050cm^{-2}

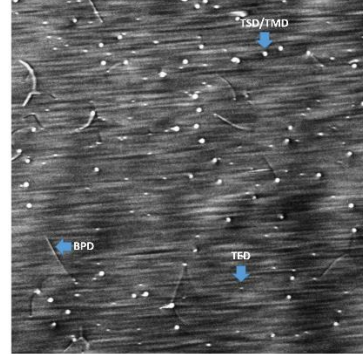Fig 3.28 Magnified image for region #3

TED:850cm^{-2}; TSD:500cm^{-2}
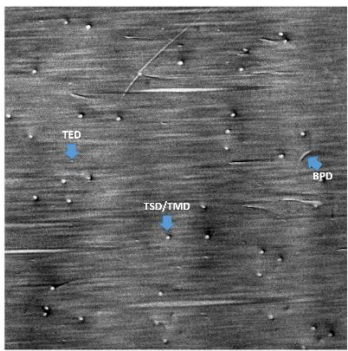
Fig 3.29 Magnified image for region #4

TED:125cm^{-2}; TSD:800cm^{-2}

Fig 3.30 Magnified image for region #5

TED:2550cm^{-2};TSD:1575cm^{-2}

Fig 3.31 Magnified image for region #6

TED:525cm^{-2}; TSD:975cm^{-2}

Fig 3.32 Magnified image for region #7
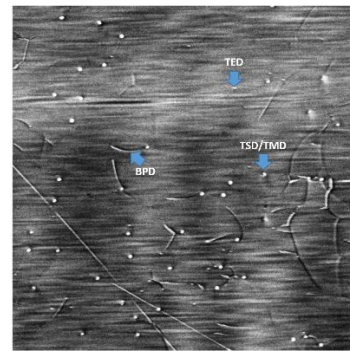
TED:600cm^{-2}; TSD:1050cm^{-2}

Fig 3.33 Magnified image for region #8
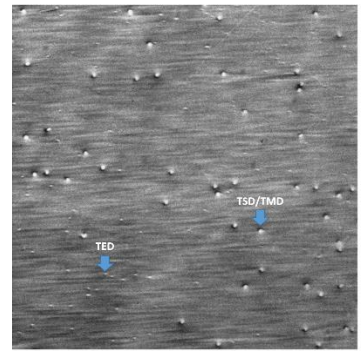
TED:2100cm^{-2}TSD:1250cm^{-2}

Fig 3.34 Magnified image for region #9

The distribution of TED and TSD of sample 2 is shown in Table 3.4

Table 3.4 Distribution of TED and TSD in sample 2

Region	1	2	3	4	5	6	7	8	9
TSD Density (cm^{-2})	325	875	1050	500	800	1575	975	1050	1250
TED Density (cm^{-2})	1700	375	725	850	125	2550	525	600	2100

The average distribution of threading dislocations is shown in Fig 3.35

Fig 3.35 Average distribution of TED and TSD/TMD, the unit is cm^{-2}

From the distribution map of threading dislocation, we could see that the density of threading dislocations on the edge of the wafer is lower than it in the center region. The reason is t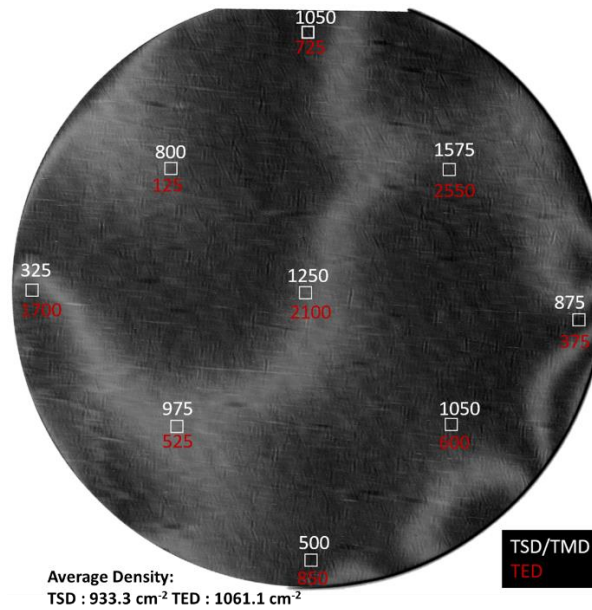hat during the growth of the crystal, at the edge of the boule, the radius of curvature is small, and there're more big growing steps to make it more steep, so when atoms deposit near big steps, it's harder to replicate the threading dislocation, and it's easier for these threading dislocations to be deflected to the basal plane, so the density of threading dislocation at the edge of the wafer is lower.

Other than the threading dislocations, we also find micropipes in grazing geometry image, indicated with red dots and arrows in Fig 3.36.
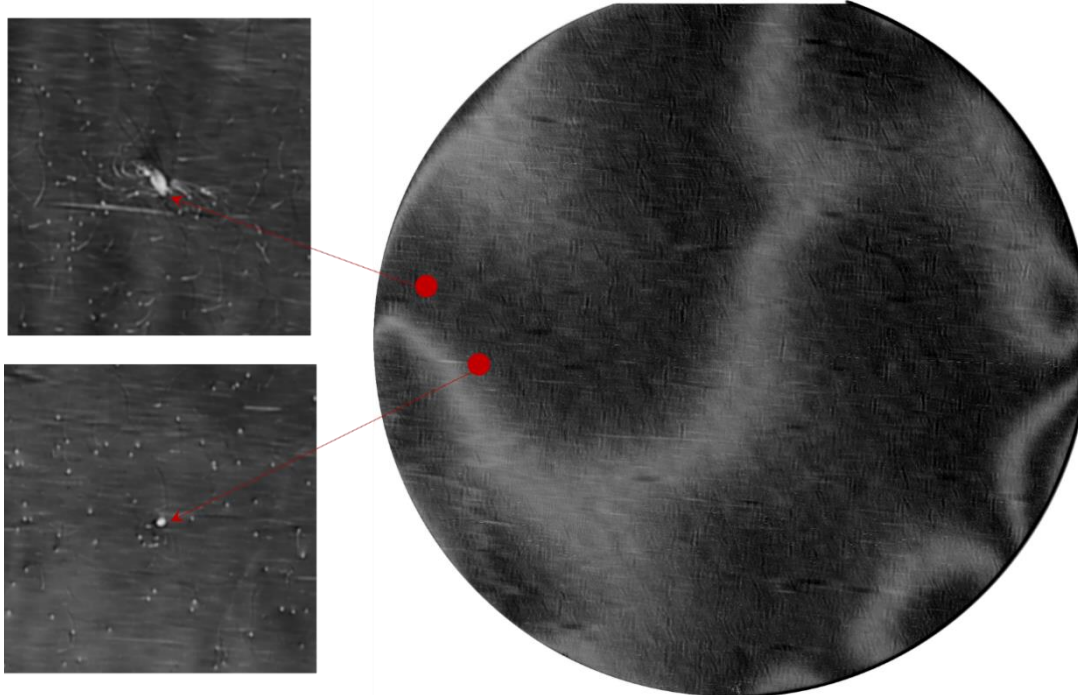
Fig 3.36 Distribution of Micropipes in grazing geometry image

Among these two micropipes, the upper left one has been observed in transmission image. It shows the same information that around the micropipe. There are groups of BPDs, since stress concentrate around MP, which make BPDs multiply and accumulate there. The comparison of this Micropipe in both transmission image and grazing image is shown in Fig 3.37 and Fig 3.38.

Fig 3.37 Micropipe in transmission image

Fig 3.38 Micropipe in grazing image

Sample 3---TYN4401503302

Sample 3 is a SiC wafer with SiC epilayer grown on the Si surface. Grazing Geometry and Transmission geometry in diffraction vectors, combined with Normaski Microscope are used to detect different kinds of defects in the sample, especially in epilayer.
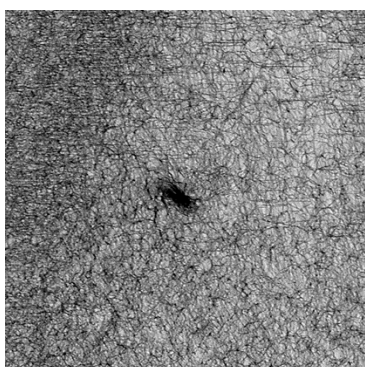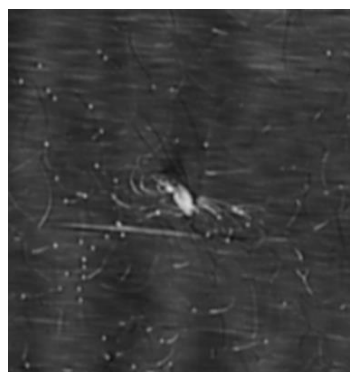
(1) Image of Sample Wafer

First we scan the wafer picture directly into the computer to search for some macro defects that could be seen by eyes. In the scanned wafer we found some 'V-shape' defects, which is magnified and shown in Fig 3.40, and the original image of whole wafer is shown in Fig 3.39. To see the V-shape defect clearly, Nomarski Microscope is used and the magnification is 1:960. The red dots on the image indicate the positions where V-shape defects are found.
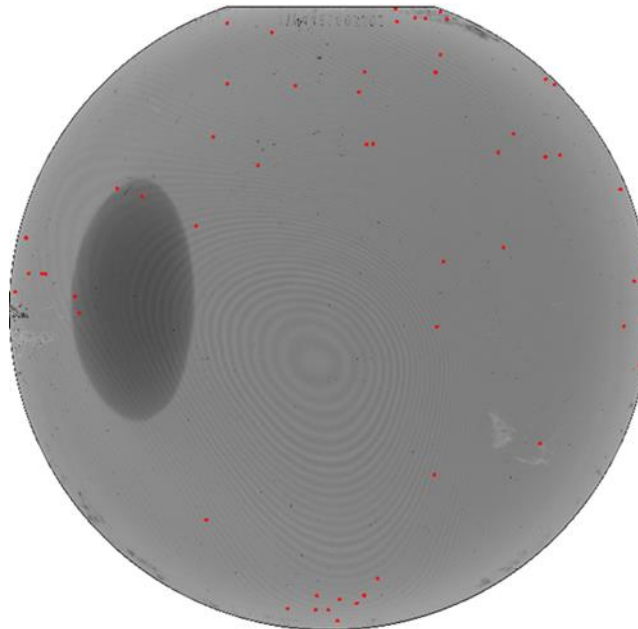

Fig 3.39 Image of scanned wafer with indication of V-shape defects positions
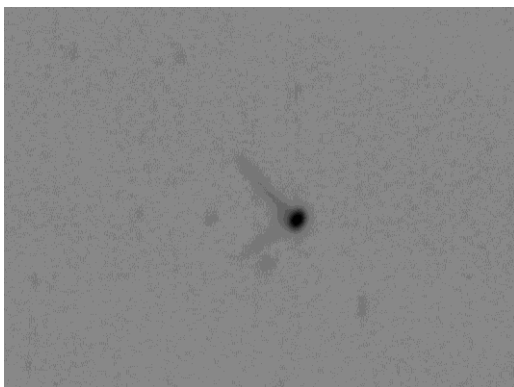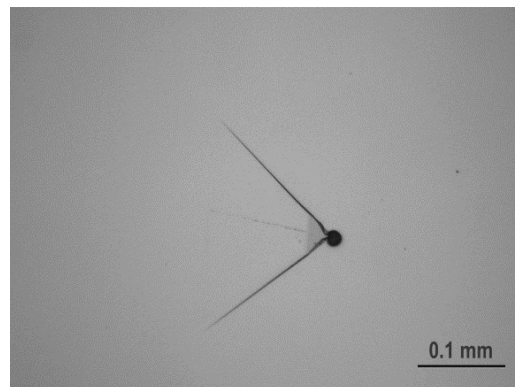

Fig 3.40 V-shape defect in scanned image

Fig 3.41 V-shape defect in Nomarski Microscope

Nomarski Microscope clearly shows that V-shape defect has a dark contrast at the head, as shown in Fig 3.41, and there're two tails following the black head, both of which can also be seen in scanned wafer image. However, with Nomarski Microscope, we could also see a region of grey contrast, just beside the black head and another tail originate between the two big tails. The distribution of V-shape defects are not uniform, and it prefer to form on the edge but not the center of the wafer.

(2) Transmission Geometry XRT On [-1-120] Diffraction

In order to learn about the V-shape defects in details, we take transmission geometry image of the same wafer. And those V-shape defects are found also in the transmission image but in a different configuration. The transmission geometry image is taken from [-1-120] diffraction and the whole wafer image is shown below in Fig 3.42. The magnified image of V-shape defects in transmission image is shown in Fig 3.43.
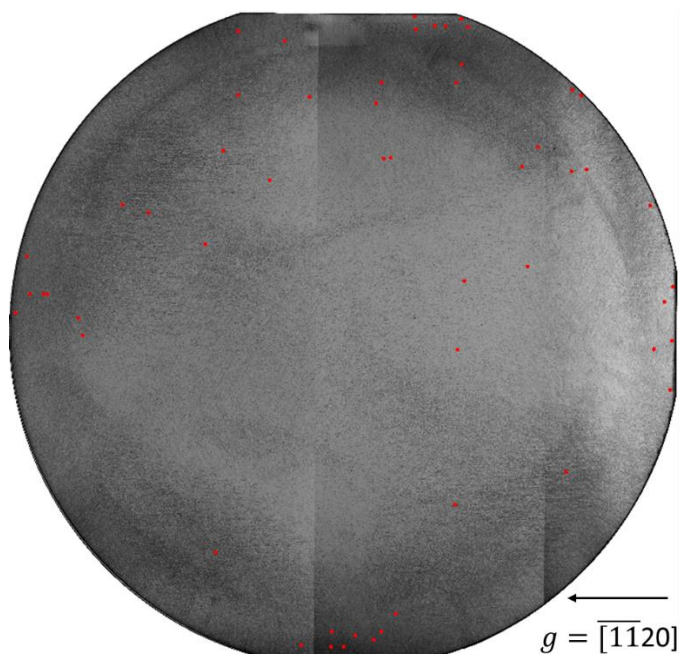

$$g = \overline{[1120]}$$

Fig 3.42 Transmission image with indications of positions of V-shape defects
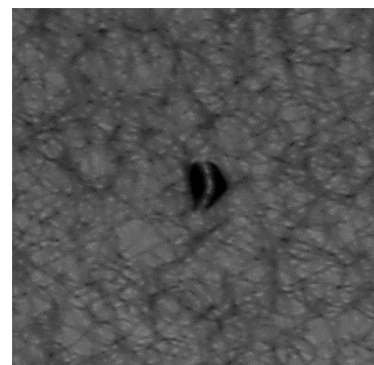
Fig 3.43   Magnified images for v-shape defects in transmission image

After looking through the whole wafer image for transmission geometry, we found all the V-shape defects that are shown in scanned wafer image. And the configuration of V-shape defect doesn't look like the one in scanned wafer. In transmission image, the V-shape defect looks like a triangle with dark contrast, and in the middle of the triangle, there's a fine line absent of the dark contrast, leaving it in a background grey contrast. The probable reason is that, contrast of transmission image only comes from the distorted lattice or misorientation along the diffraction direction, if the distortion is vertical to the diffraction direction, there won't be any contrast. For example, the image above is taken on [-1-120] diffraction, then only the change of interplane spacing of (-

11-20) plane could be revealed by the contrast, if the stress field around this defect doesn't change the lattice spacing between (-1-120) planes, there will be no contrast. So for this V-shape defect, the stress field in the middle of this defect might not change the (-1-120) plane space, then this small part shows no contrast.

(3) Grazing Geometry Monochromatic Synchrotron XRT

Another method to detect this V-shape defect is grazing geometry monochromatic synchrotron XRT. The diffraction vector is [-1-128], and the configuration of the V-shape defect is shown in Fig 3.44.
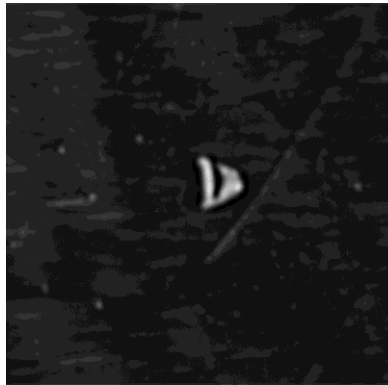

Fig 3.44 V-shape defect in grazing geometry image

From the grazing image we could see that V-shape defect looks like it in the transmission image, but the contrast is opposite. The whole defect is white contrast and the middle part is dark contrast.

(4) Transmission Geometry XRT On [1-100] and [1-101] Diffraction

In the previous chapter, we've talked about that dislocations in the substrate and V-shape defects in the epilayer. Next we'll talk about another common defect that could be found in epilayer, stacking fault. To see stacking fault, we need specific diffraction vector. We take the transmission geometry image with both [1-100] and [-1101] diffraction to characterize stacking fault in SiC epilayer. The images are shown in Fig 3.45 and Fig 3.46.

$\uparrow g = 1\bar{1}00$ $\downarrow g = \bar{1}101$
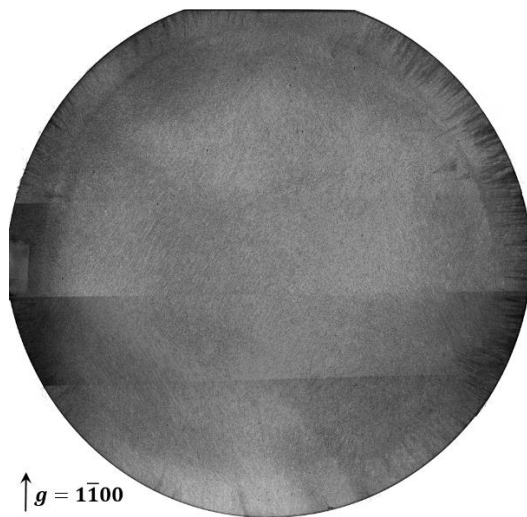
Fig 3.45 Transmission geometry image with [1-100]diffraction   Fig 3.46 Transmission geometry image with [-1101]diffraction
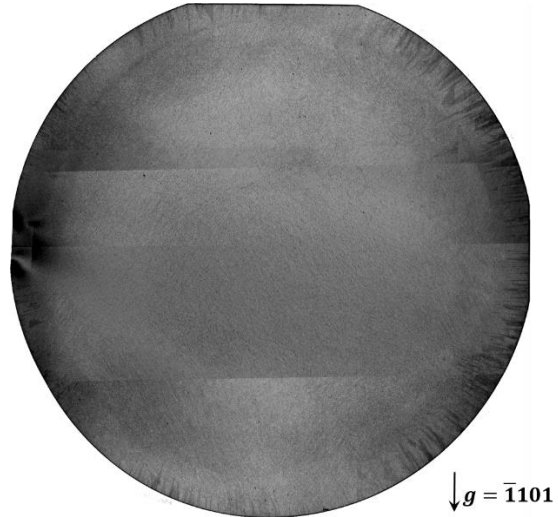
From these two images with two diffraction vector, we see some triangle dark contrast on the edge of the images, which are Frank stacking faults and Shockley stacking fault. Since different stacking faults have different burger's vector, and if $g \cdot b = 0$, the stacking fault will disappear in the image. For Frank stacking fault, the burger's vector is 1/2 <0001>, and it will disappear on [1-100] diffraction but show up in [-1101] diffraction. For Shockley stacking fault, the burger's vector is 1/3 <1-100>, and it will show up both in [1-100] and [1-101] diffraction. In order to count all the sacking fault in the wafer, we combine these two image together, and calculate the percentage of stacking fault that occupy the whole wafer. We use area percentage to evaluate, and with the help of Program Spot, we can measure the area of all the triangle dark contrast on each image, and subtract the overlapped part, then get the final result of the stacking fault area. At last divide this value by the area of the whole wafer, a 4-inch circle, which is 8103.2 mm^2, we will get the percentage of stacking fault. After measurement, we get the area of stacking fault is 399.5 mm^2 and the percentage is 0.493%

3.4 Conclusion

A combination of techniques like transmission geometry synchrotron XRT, grazing geometry synchrotron XRT and Nomarski Microscope is used to detect the defects in SiC single crystal. Basal Plane Dislocation, Prismatic Dislocation, Threading Edge Dislocation, Threading Screw Dislocation, V-shape Defect and Stacking Faults are characterized. Dislocation density is calculated, and the origins of the dislocation distribution is analyzed.

Chapter 4. Introduction of GaN

4.1 Structure of GaN

Similar with SiC, GaN is also hexagonal structure. And the coordination geometry of GaN is tetrahedral, which means one Gallium atom is connected with four Nitride atoms by covalence bond and one Nitride atom is also connected with four Gallium atom in the same way. This tetrahedron repeats its position every two layer, so the general structure of GaN can be seen as two simple hexagonal lattice structure, one set of gallium atoms and one set of nitride atoms, superimposed with each other, with a 3/8 shift on [0001] axis. The stick and ball model of GaN is shown in Fig 4.1, and Fig 4.2[20], and it's the projection of GaN stick and ball model in [11-20] direction.
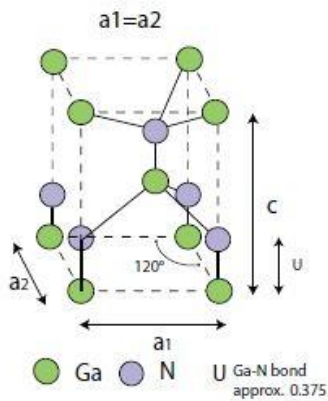

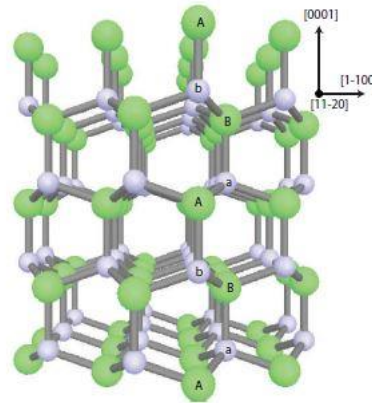Fig 4.1 Stick and ball model of GaN, and U stands for the bond between Ga atom and N atom

Fig 4.2 Projection of GaN structure on [11-20] direction

From Fig 4.1 we can see clearly that the set of purple balls are in the same positions with the green balls, but just a distance U higher than the green balls. U is the distance between Ga atom and N atom, which is 3/8 (0.375) of c. And from Fig 4.2, we see the stacking sequence of (0001) plane in GaN structure is ABABA… for Ga atoms, and is ababa… for N atoms. Obviously, it's a two-layer repeated structure, and this structure is named as Wurtzite Structure, which is also possessed by wurtzite itself, ZnO, AlN, InN, α-SiC and many other semiconductor materials. Some parameters of different wurtizite structure materials is shown below in Table 4.1.

Table 4.1 Parameters of wurtzite structure materials [20]

Parameter	GaN	AlN	InN
Lattice constant (nm)	a=0.319; c=0.518	a=0.311; c=0.498	a=0.354; c=0.572
U	0.375	0.382	0.379
Thermal Expansion Coefficient(K^{-1})	a=0.59*10^{-6} c=3.17*10^{-6}	a=4.15*10^{-6} c=5.27*10^{-6}	a=3.8*10^{-6} c=2.9*10^{-6}

4.2 Property and Application of GaN

According to Table 1.1, when compared with Si and GaAs, GaN has a higher saturation drift velocity, which is 2.5 x 10^7 cm/s. And it also have a high band-gap, 3.4eV, which is even higher than SiC and higher breakdown field. All of these make GaN a good materials to be applied in optoelectronic high-power and high-frequency devices, such as LED and GaN-based MOSFET or MESFET[21][22].

Chapter 5 Characterization Technique for GaN Crystal

In the research of defects in GaN crystal, Synchrotron X-ray Topography is also used. The mechanism of XRT is discussed in Chapter 2. Another technique used to detect the defects in GaN is High Resolution X-ray Diffraction (HRXRD), and one software program HXRD is used to help analyze the data from HRXRD. Next the mechanism and the details of HRXRD and the software will be discussed.

5.1 High Resolution X-ray Diffraction (HRXRD)

As we mentioned at the end of chapter 2, when x-ray is diffracted by crystal, there's a narrow range around the Bragg angle, over which x-ray beam can be diffracted, and this range is indicated as $\Delta\theta$ or rocking curve width. As shown in Table 2.2, different planes have different $\Delta\theta$, which is also decided by wavelength and absorption coefficient. HRXRD is a technique for measuring the exact $\Delta\theta$ for different plane in a crystal. The set-up we use for HRXRD measurements is called Bede D1 System. First, the electrons are accelerated by high voltage, then the high speed electrons hit the target metal, which is Copper, to activate the Kα characteristic radiation, after the radiation passing through a film with certain absorption limitation, very narrow spectrum is retained. And next we put a monochromator on the path of the beam, after exiting from the monochromator, the beam is monochromatic and we can use it for performing the rocking curve experiment. The monochromator inside the machine is Germanium with (0004) as the surface plane. The energy for the electronic beam in this device is 30 KeV, and the emitting Cu Kα radiation is 8.05 KeV. The configuration of Bede D1 System is shown in Fig 5.1.
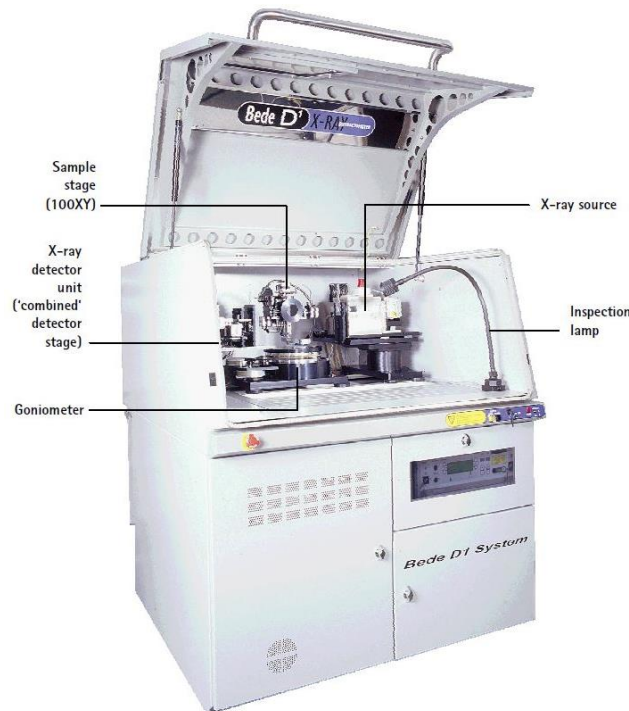

Fig 5.1 Bede D1 System used for High Resolution X-ray Diffraction

From the configuration picture, we could see that after x-ray become monochromatic, it hits the sample mounted on the sample stage, and then the signal will be absorbed by the detector behind it. First we need to decide the plane we want to measure, typically the surface plane, and calculate the Bragg angle for the Cu K$_\alpha$ energy, then set the sample stage and detector to the position that match the angles we calculated, at last we do a scan of omega, which is the angle between incident beam and sample surface, within a range about 1800'' around the theoretical value we just calculated. The intensity of diffracted beam is recorded by the detector and is converted to electronic signal shown as a graph, which relates the omega angle with the intensity of diffracted beam. The configuration of sample stage and detector is shown in Fig 5.2 and Fig 5.3.
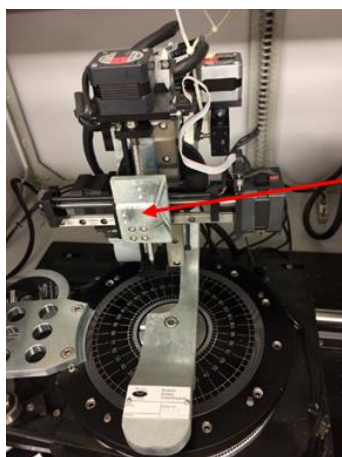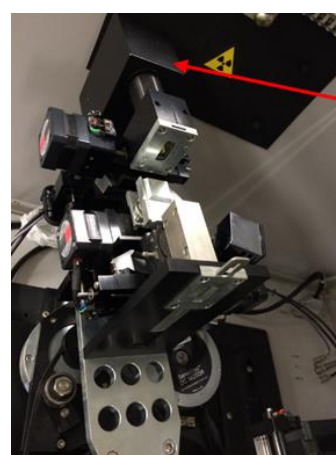

Fig 5.2 Sample stage with goniometer

Fig 5.3 X-ray Detector

5.2 Application of HXRD Software

In the previous section we discussed the measurement of rocking curve of a real crystal. To evaluate the crystalline quality, we also need the rocking curve from a perfect crystal, and compare these two rocking curves to get the result about range of misorientations. Since we don't have access to a perfect crystal, we use a software called HXRD to simulate the ideal rocking curve [23]. The details about the application of this software is shown in Fig 5.4. In order to get the rocking curve, you should provide several parameters as following:

(1) The Photon Energy---This is decided by the wavelength of incident x-ray beam. In this experiment, we use copper as the target metal, and Kα radiation as the incident beam. The wavelength of it λ=1.54056 Å, and the energy of it is 8.048 KeV.
(2) Thickness of the sample
(3) Crystal Structure---In this experiment, all the samples we use are GaN
(4) Diffraction Plane (HKL)----We use samples with three typical geometry, c plane as the surface, which is (0001), m plane as the surface, which is (1-100), and a plane as the surface, which is (11-20). For c plane sample, the diffraction is a little bit

changed, because the structure factor of hexagonal GaN doesn't allow diffraction from plane (hkl), if h + 2k = 3n and l= odd. So we use (0002) as the diffraction plane. For m plane sample, we use (100) plane as the diffraction plane, because (100) plane is equal to (10-10) plane in hexagonal structure, which is equivalent plane with (1-100). For a plane sample, we just use (110) as the diffraction plane , which is also the surface plane.

(5) Bragg Angle θ_B --- According to Bragg's Law, $2d_{hkl} \sin \theta_B = \lambda$, when we decide the wavelength of incident beam and the diffraction plane (hkl), we can calculated the specific Bragg angle for each plane.
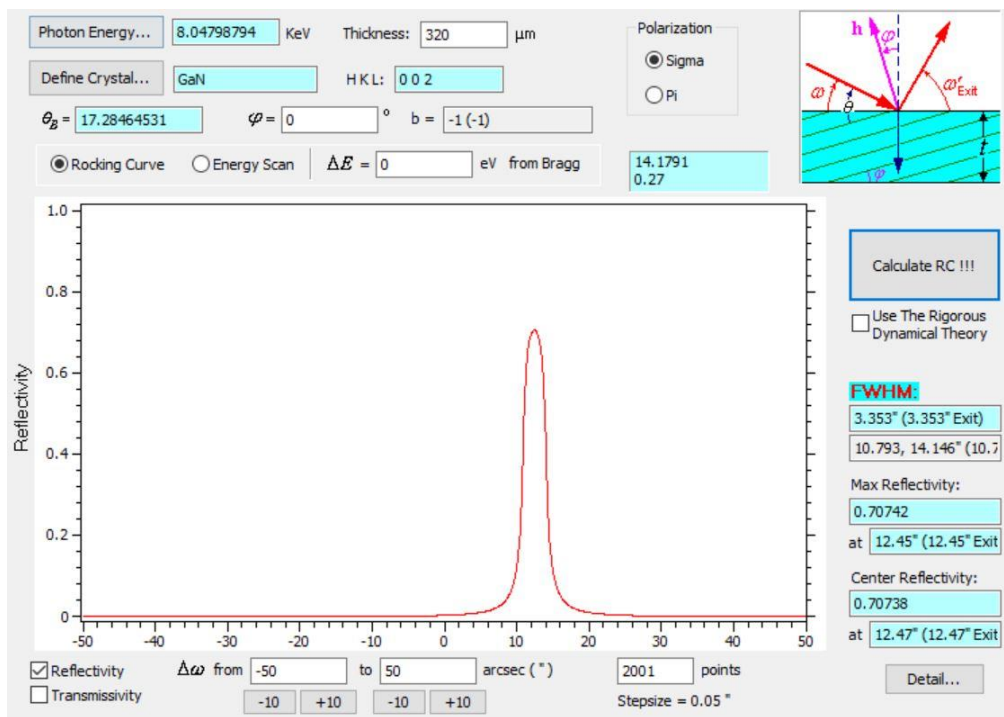
Fig 5.4 Rocking curve of perfect crystal with plane wave diffraction

After entering all the parameters, the simulated rocking curve will show up on the screen, along with information about reflectivity, including Full Width Half Maximum (FWHM) of the rocking curve, which is the most important, which is indicated as $\triangle\theta$ of the rocking curve.

This result is for diffracted beam intensity from a plane wave, which means there's no divergence for the beam. But in reality, the x-ray generated from a lab source are inherently divergent even after going through a channel-cut monochromator. So we change to double crystal diffraction rocking curve for divergent incident beam. In this mode, other than the information of the sample, we also need to provide the details about the monochromator. In this experiment, we use channel-cut Ge single crystal as the monochromators with the surface (0004) plane. The indication of this mode is shown in Fig 5.5, and the corresponding simulated rocking curve is a convolution of monochromator and sample crystal rocking curves.
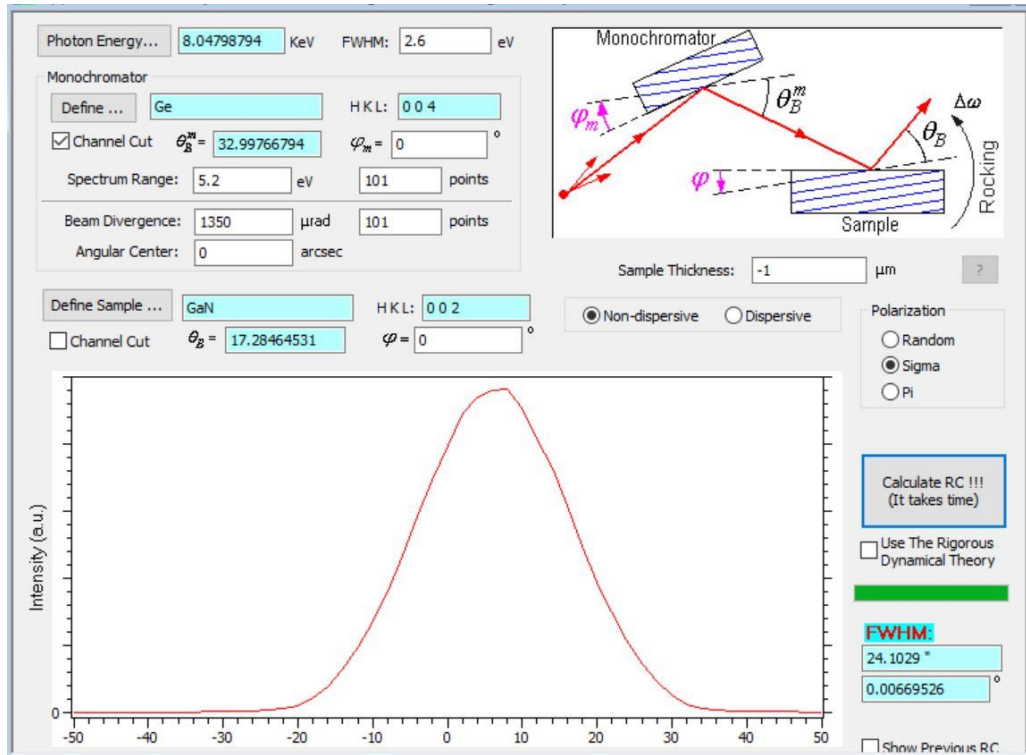
Fig 5.5 Rocking curve of perfect crystal with divergent beam diffraction

Chapter 6. Defect study of GaN Crystal

6.1 Introduction

In this chapter, 8 samples are analyzed in detail. These are all bulk GaN crystals. Four of them are c plane samples, which means (0001) plane is the surface plane, two of them are m plane samples with (1-100) plane as the surface, and the other two samples are a plane samples with (11-20) as the surface. In the experiment, HRXRD is used to measure the rocking curve of these crystals and then comparing with ideal rocking curve that is simulated by software HXRD. The Full Width Half Maximum (FWHM) is measured, because it represents for the defects density, mainly sub-grain boundary, the higher FWHM is, the more sub-grain boundary there is.

6.2 Results and Discussion

6.2.1 C-Plane Samples

As we discuss in the last chapter, for c plane sample, we use (0002) as the diffraction plane. The ideal rocking curve with plane-wave beam diffraction and divergent beam diffraction that simulated by software are shown in Fig 6.1 and Fig 6.2.
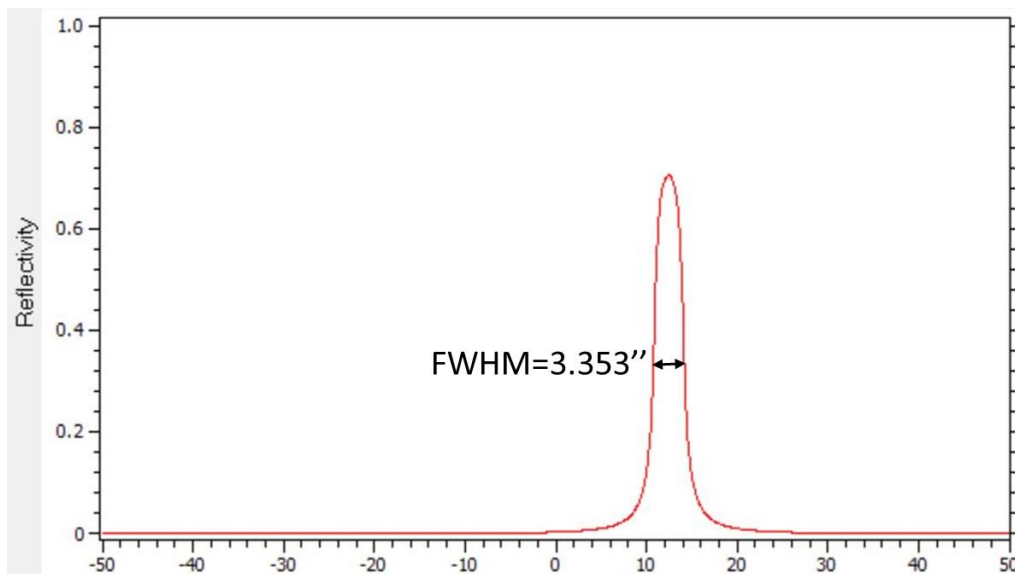
Fig 6.1 Simulated rocking curving with plane-wave beam diffraction of perfect c plane GaN crystal
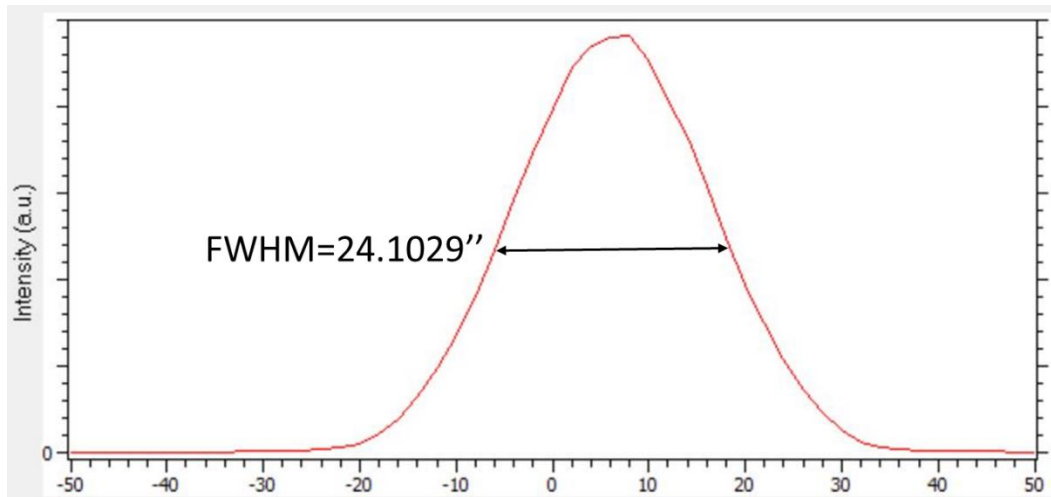
Fig 6.2 Simulated rocking curve with divergent beam diffraction of perfect c plane GaN crystal

Sample 1----S#A

The picture of sample 1 is shown in Fig 6.3. The dimension of it is 5mm x 10mm, and the thickness is 320 μm. We did Omega Scan in three positions of the sample, which are indicated by the red dots. Make the center point of the sample as the origin point, and the coordinates are (0,0) (0,3) (0,-3). The graphs of omega scan in three positions are shown in Fig 6.4.
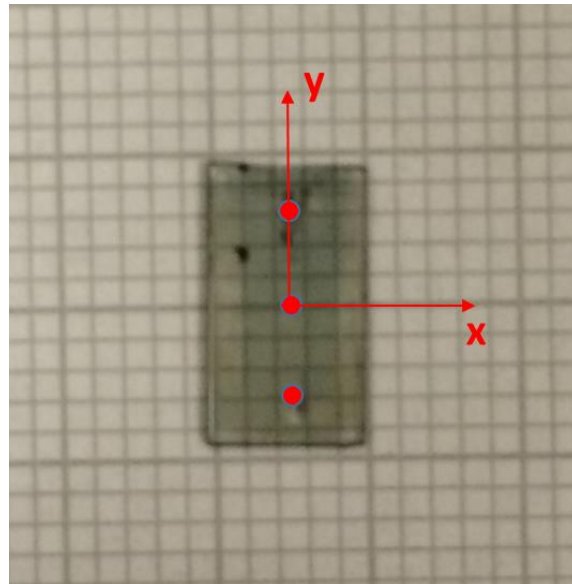

Fig 6.3 The picture of Sample one with three positions indicated by red dots
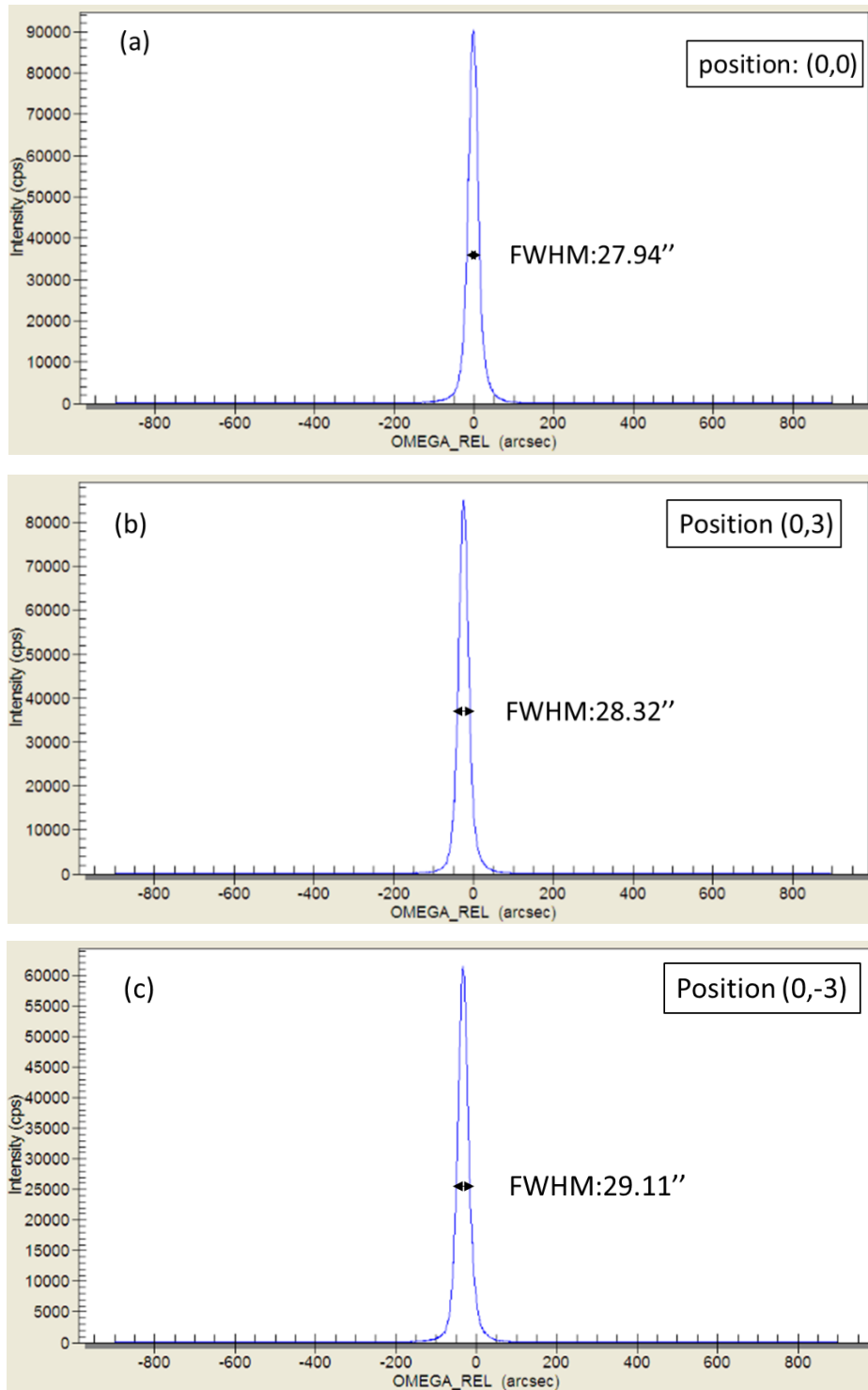
Fig 6.4 Omega Scan of Sample 1 in (a) (0,0) position; (b) (0,3) postion; (c) (0,-3) postion

Sample 2---S#B

The picture of sample 2 is shown in Fig 6.5. The dimension of it is 5mm x 7mm, and the thickness is 300 μm. Similarly, we also did omega scan on three position which are (0,0) (0,3) (0,-3) and the graph is shown in Fig 6.6.
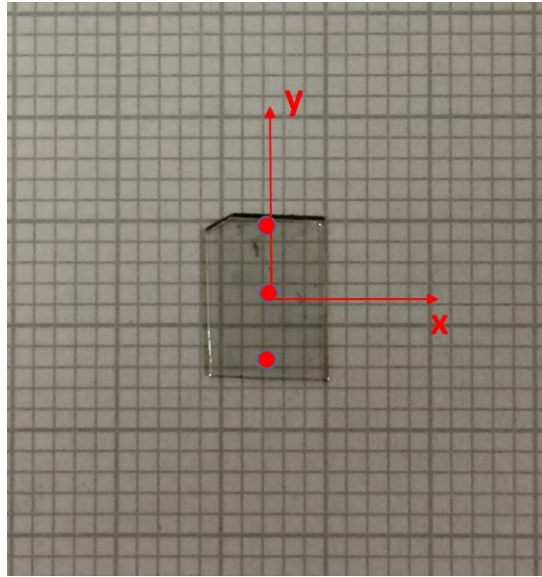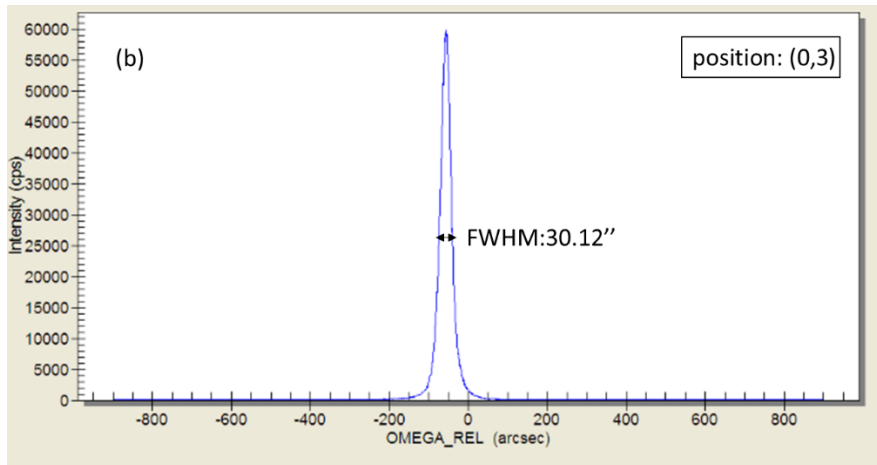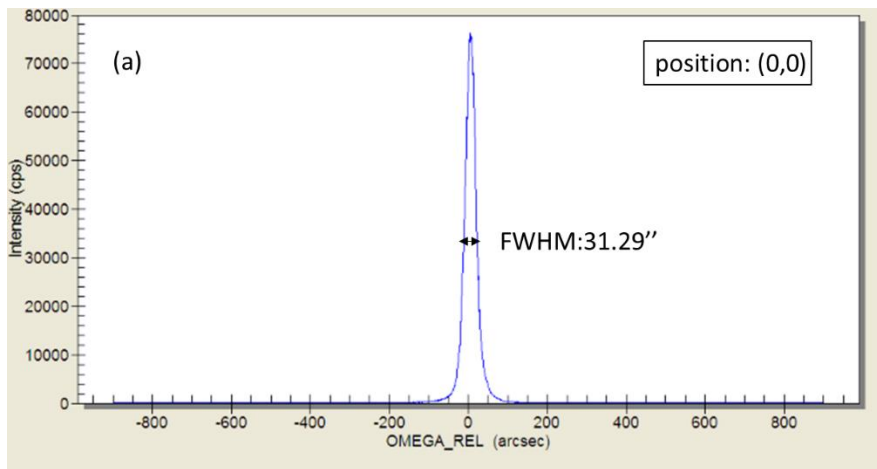
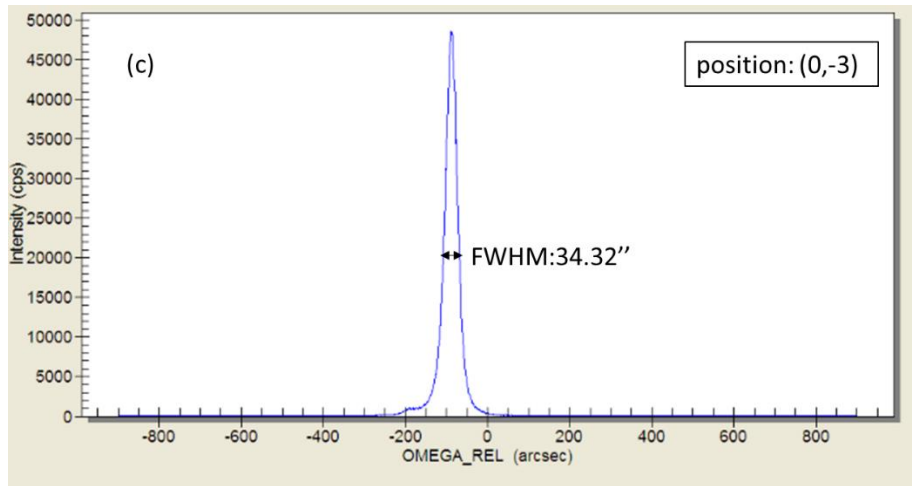Fig 6.5 The picture of Sample 2 with three positions indicated by red dots

Fig 6.6 Omega Scan of Sample 2 in (a) (0,0) position; (b) (0,3) postion; (c) (0,-3) postion

Sample 3---X6452

The picture of sample 3 is shown in Fig 6.7. The dimension of it is 10mm x 10mm. We did omega scan on three position which are (0,0) (3,0) (-3,0) and the graph is shown in Fig 6.8.
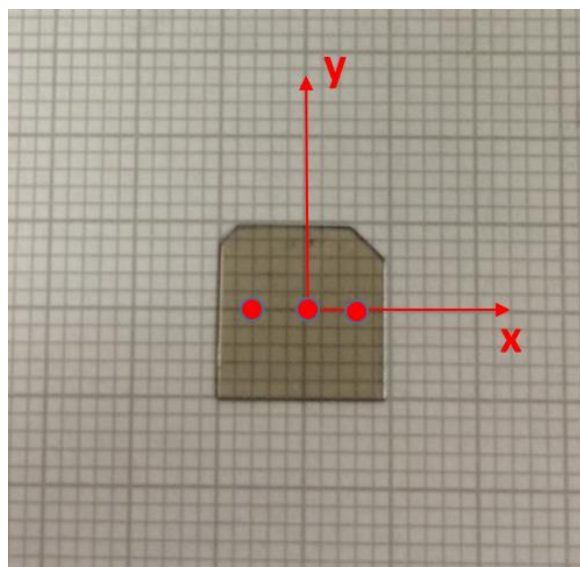

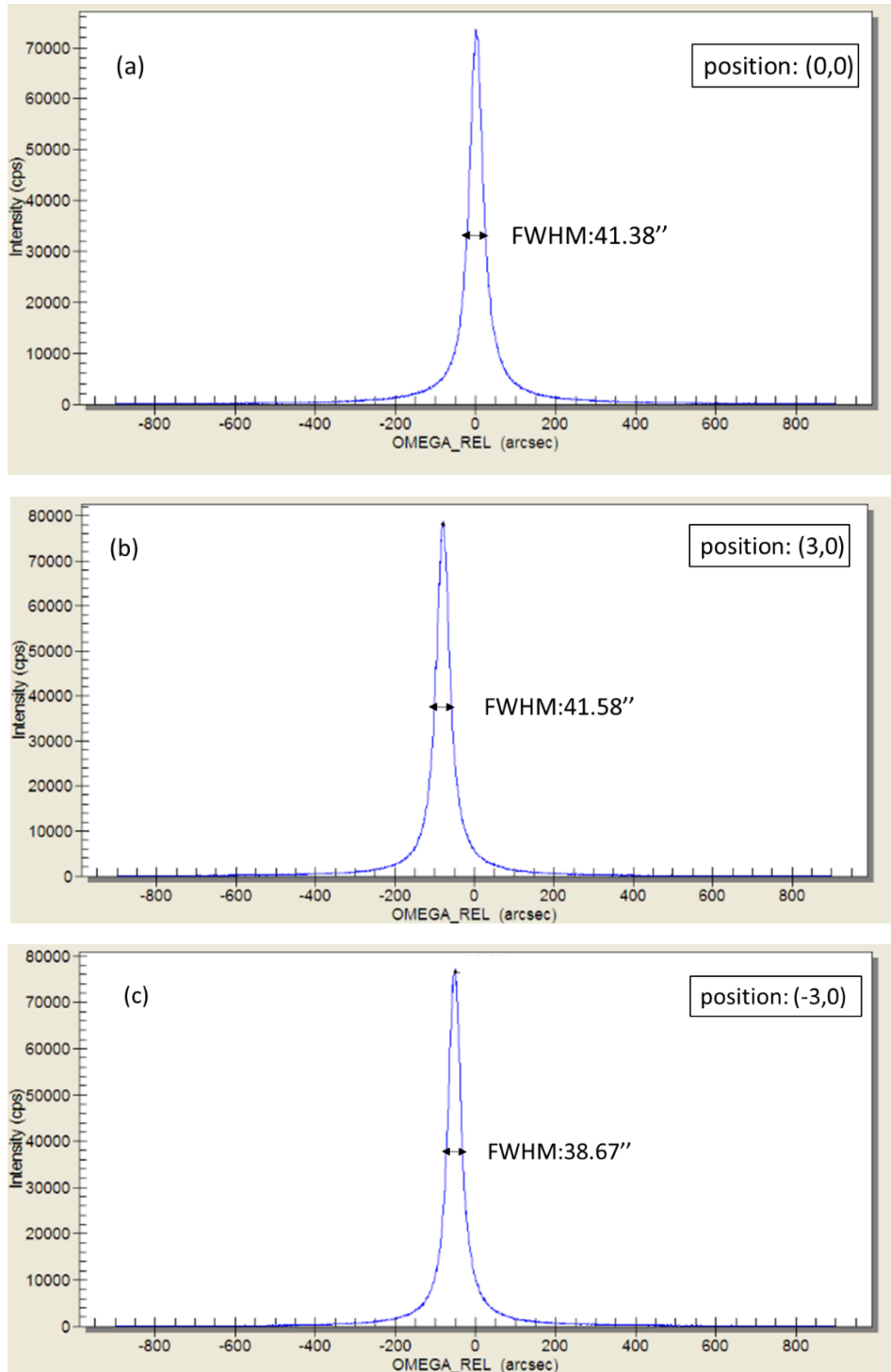Fig 6.7 The picture of Sample 3 with three positions indicated by red dots

Fig 6.8 Omega Scan of Sample 2 in (a) (0,0) position; (b) (3,0) postion; (c) (-3,0) postion

Sample 4---X2362

The picture of sample 4 is shown in Fig 6.9. The dimension of it is 10mm x 10mm. We also did omega scan on three position which are (0,0) (3,0) (-3,0) and the graph is shown in Fig 6.10.
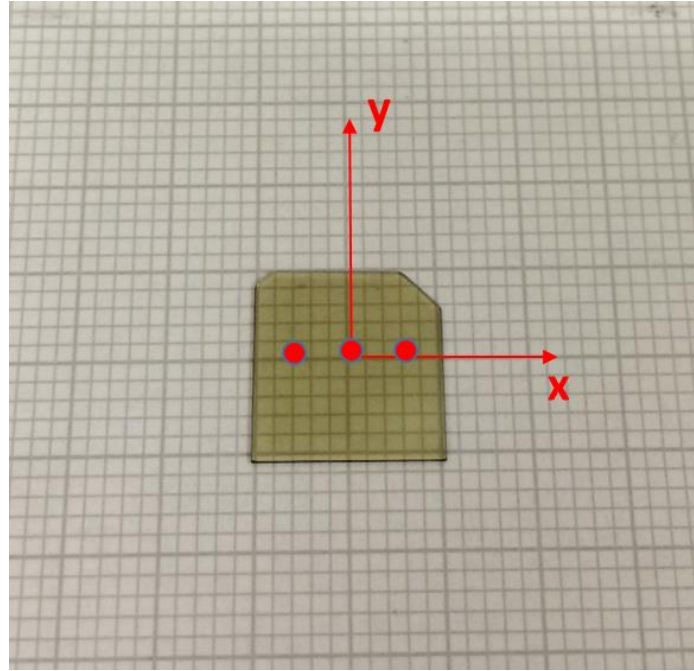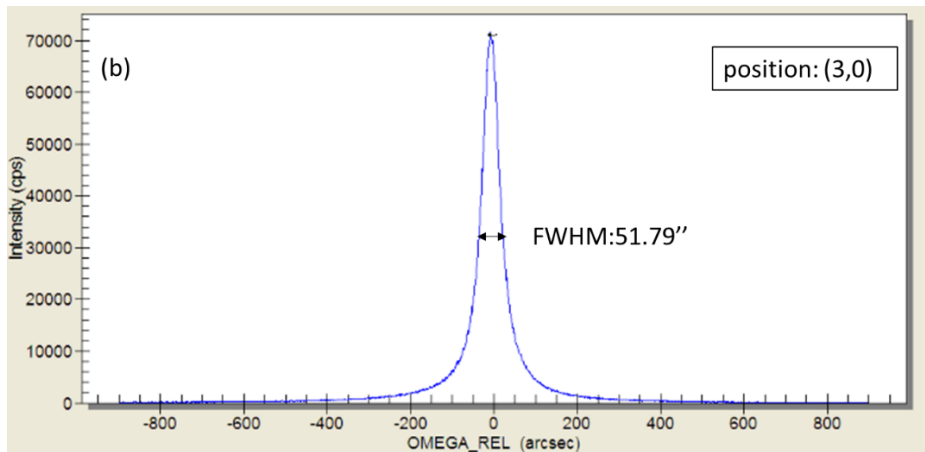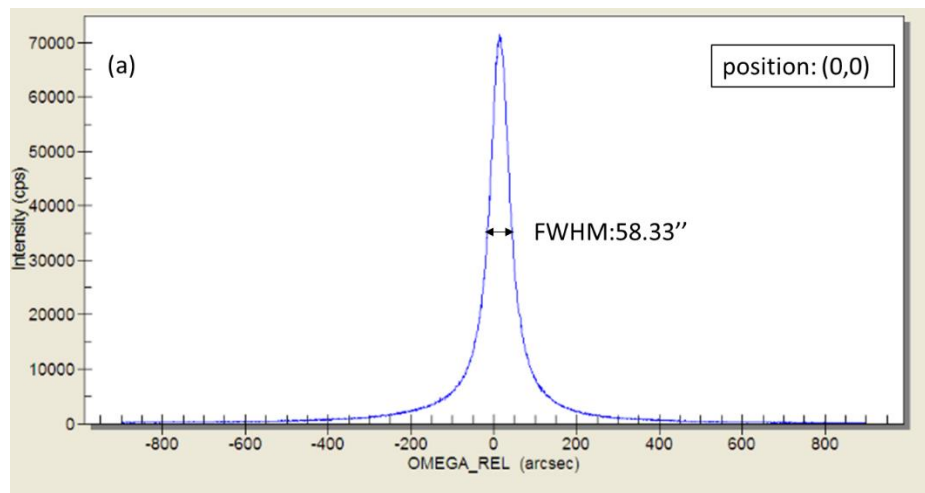
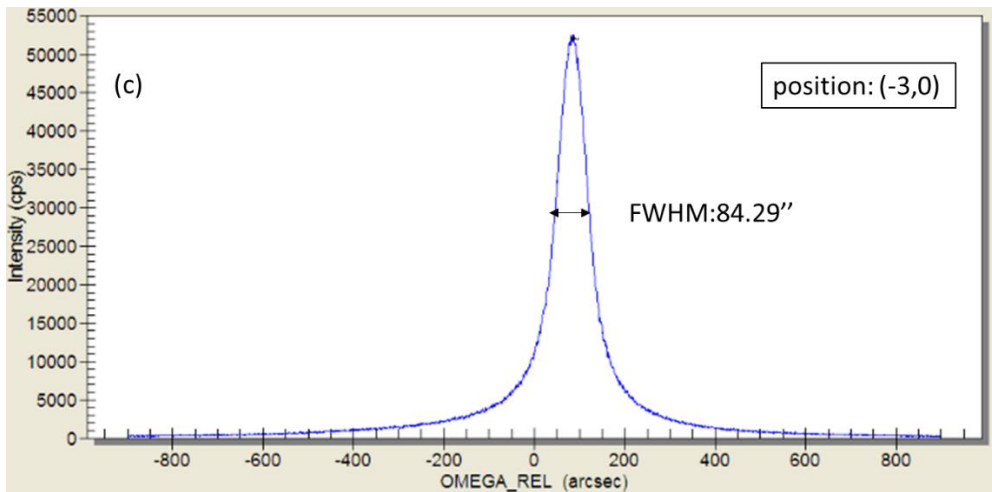Fig 6.9 The picture of Sample 4 with three positions indicated by red dots

Fig 6.10 Omega Scan of Sample 4 in (a) (0,0) position; (b) (3,0) postion; (c) (-3,0) postion

6.2.2 M-plane Sample

For m-plane sample the diffraction plane is (100), and the ideal rocking curve with plane-wave beam diffraction and divergent beam diffraction that simulated by software are shown in Fig 6.11 and Fig 6.12.
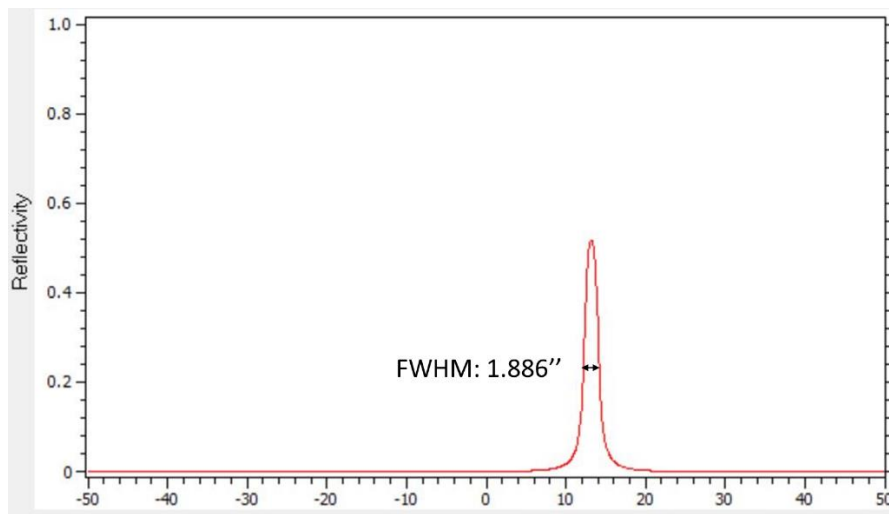

Fig 6.11 Simulated rocking curving with plane-wave beam diffraction of perfect m plane GaN crystal
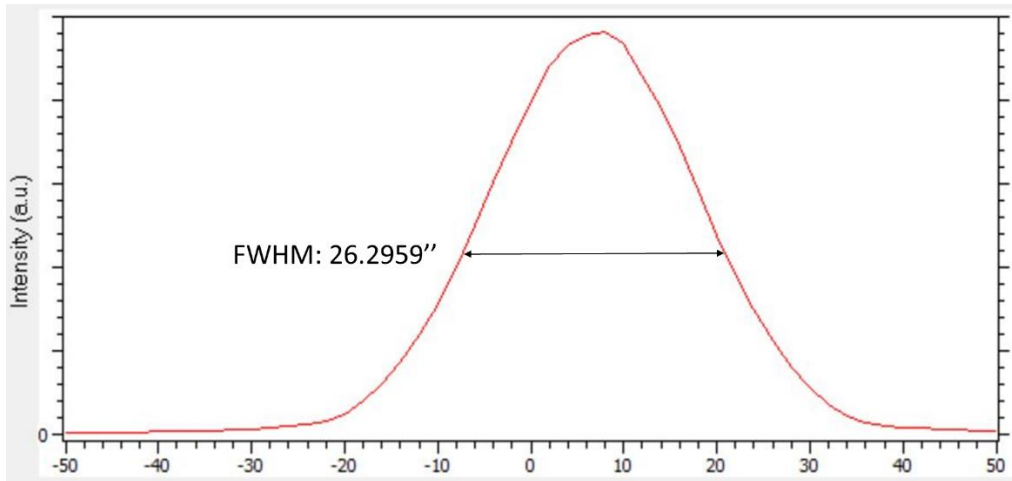
Fig 6.12 Simulated rocking curving with divergent beam diffraction of perfect m plane GaN crystal

Sample 5----Y5252

The picture of sample 5 is shown in Fig 6.13. The dimension of it is 10mm x 10mm. We did omega scan on three positions which are (0,0) (2,0) (-2,0) and the graph is shown in Fig 6.14.
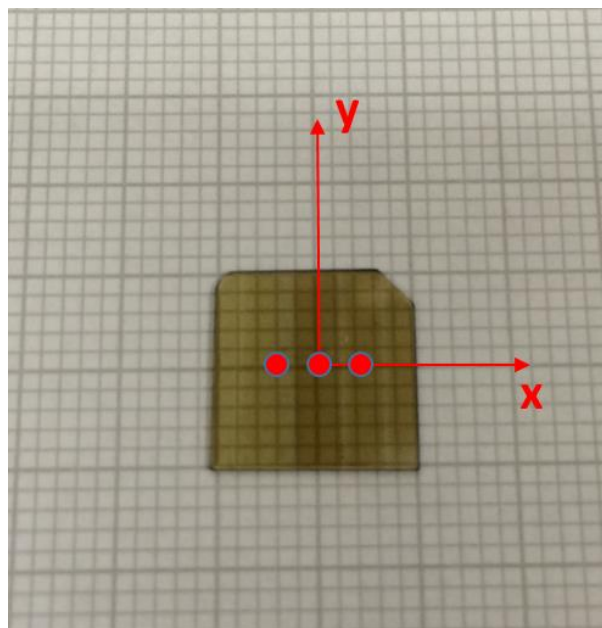

Fig 6.13 The picture of Sample 4 with three positions indicated by red dots
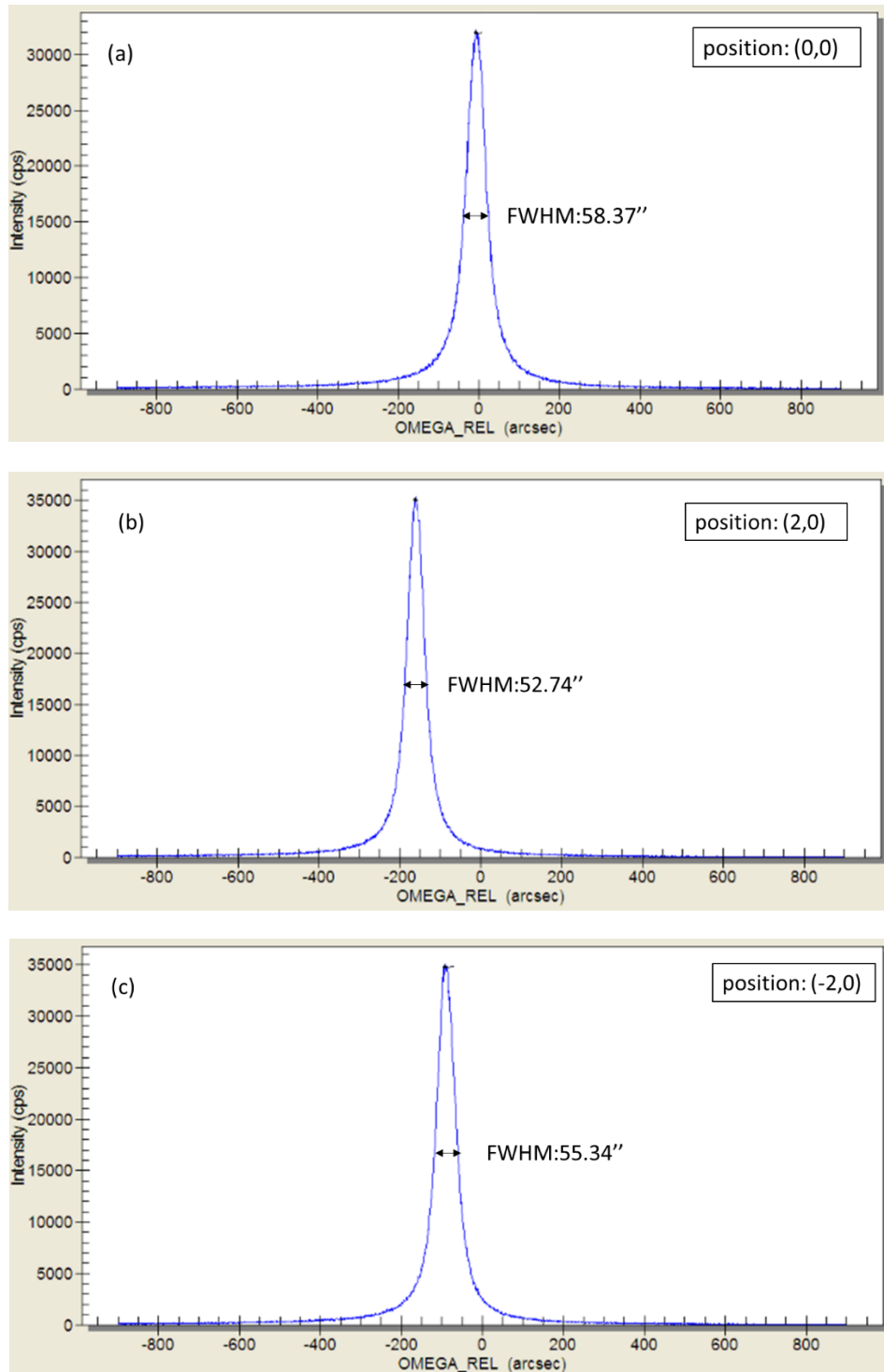
Fig 6.14 Omega Scan of Sample 5 in (a) (0,0) position; (b) (2,0) postion; (c) (-2,0) postion

Sample 6----Y4923

The picture of sample 6 is shown in Fig 6.15. The dimension of it is 10mm x 13mm. We did omega scan on three positions which are (0,0) (0,4) (0,-4) and the graph is shown in Fig 6.16.
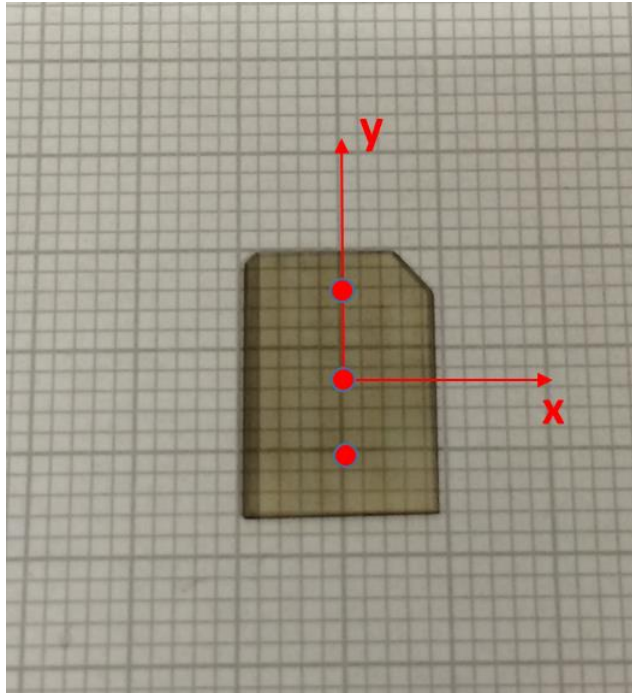
Fig 6.15 The picture of Sample 6 with three positions indicated by red dots
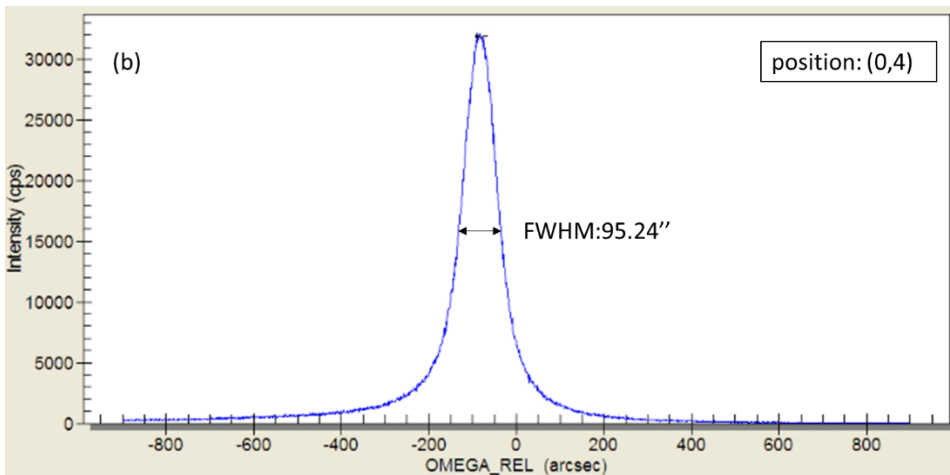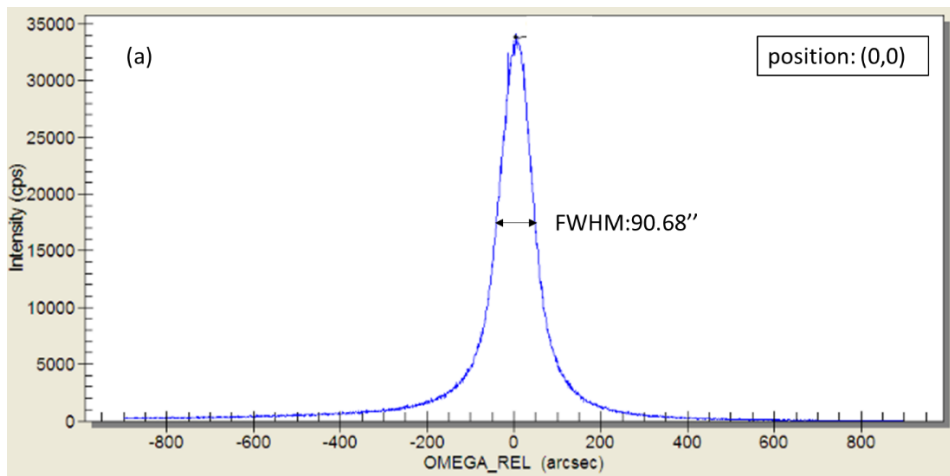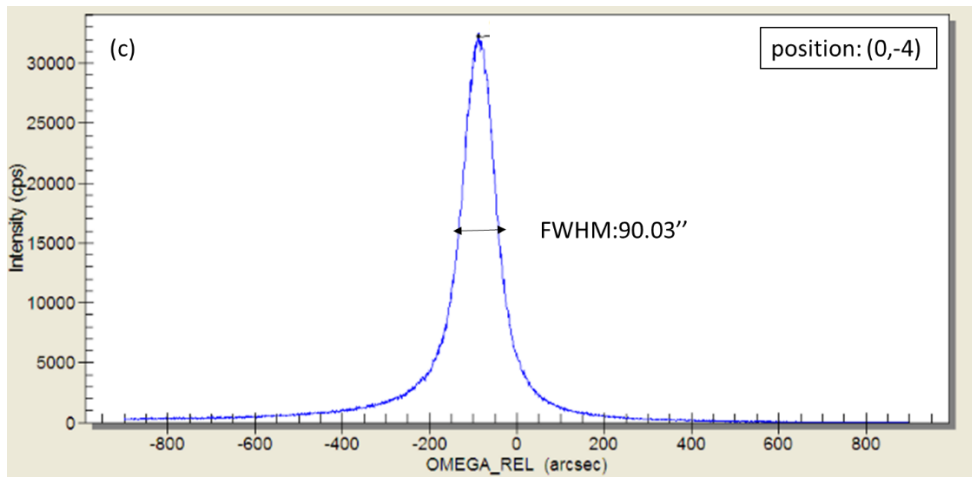
Fig 6.16 Omega Scan of Sample 6 in (a) (0,0) position; (b) (0,4) postion; (c) (0,-4) postion

6.2.3 A-plane Sample

For a-plane sample the diffraction plane is (110), and the ideal rocking curve with plane-wave beam diffraction and divergent beam diffraction that simulated by software are shown in Fig 6.17 and Fig 6.18.
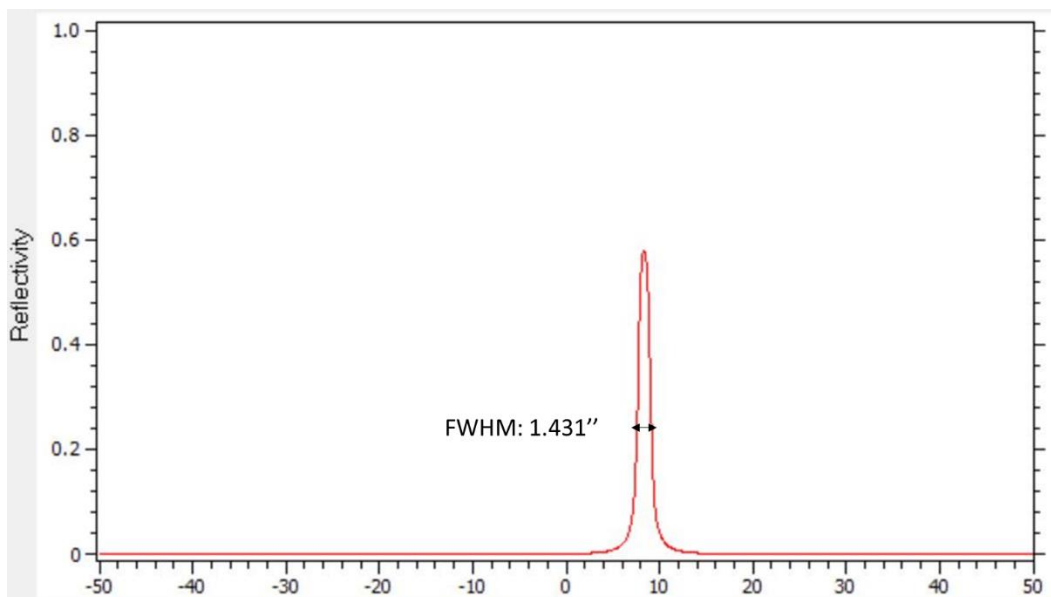
Fig 6.17 Simulated rocking curving with plane-wave beam diffraction of perfect a plane GaN crystal
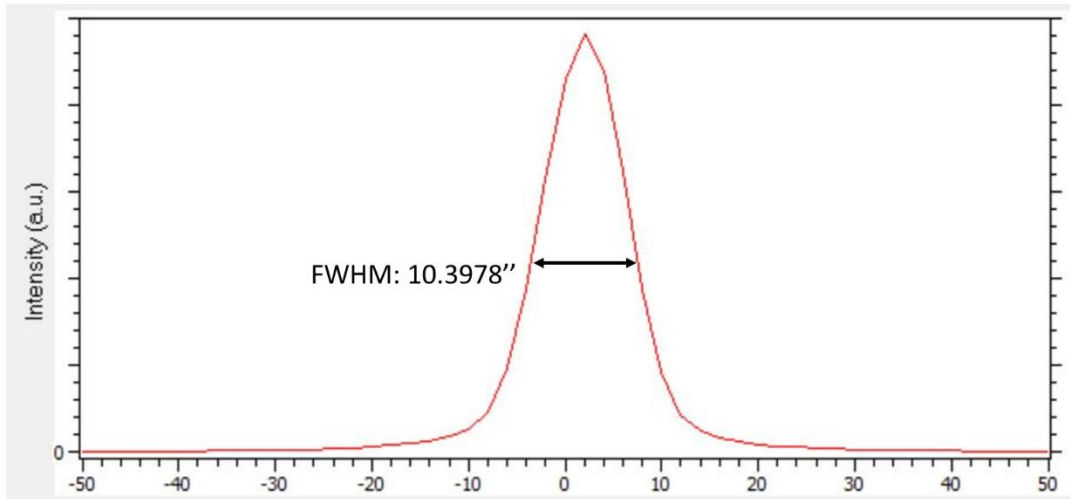
Fig 6.18 Simulated rocking curving with divergent beam diffraction of perfect a plane GaN crystal

Sample 7----Z5262

The picture of sample 7 is shown in Fig 6.19. The dimension of it is 10mm * 10mm. We did omega scan on three positions which are (0,0) (0,3) (0,-3) and the graph is shown in Fig 6.20.
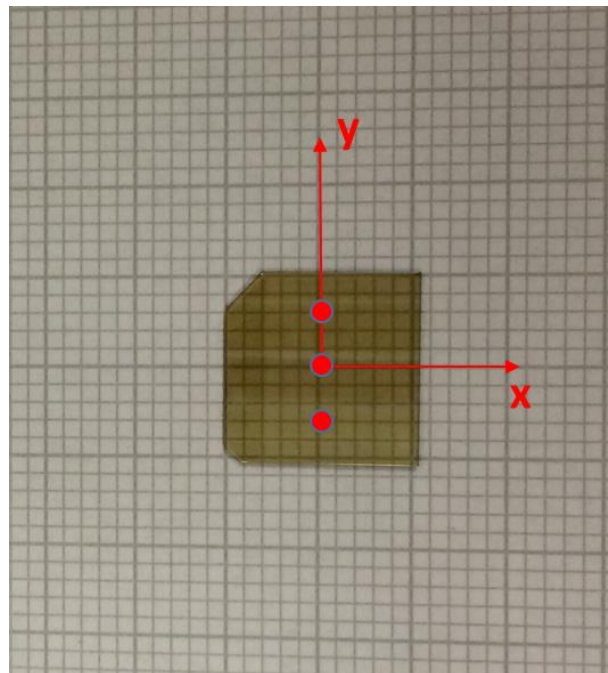

Fig 6.19 The picture of Sample 7 with three positions indicated by red dots
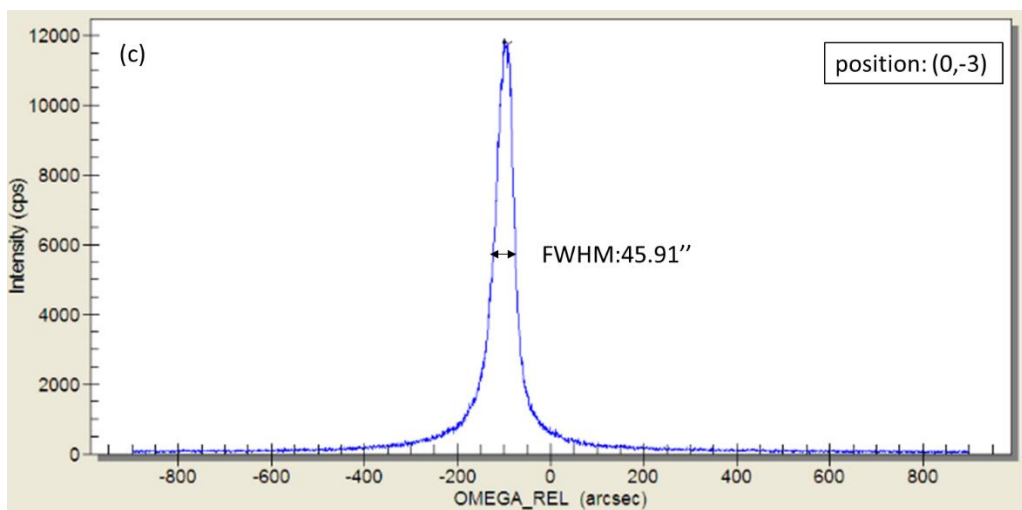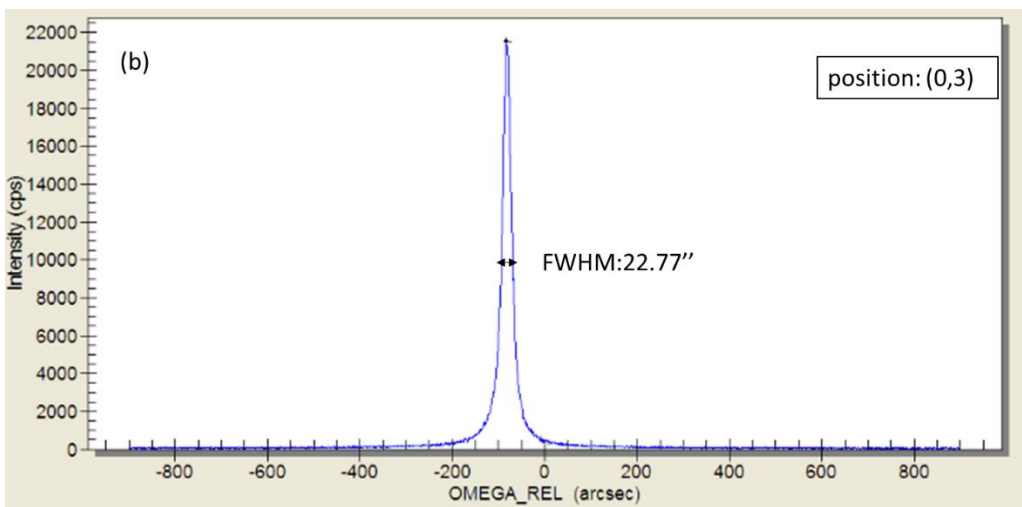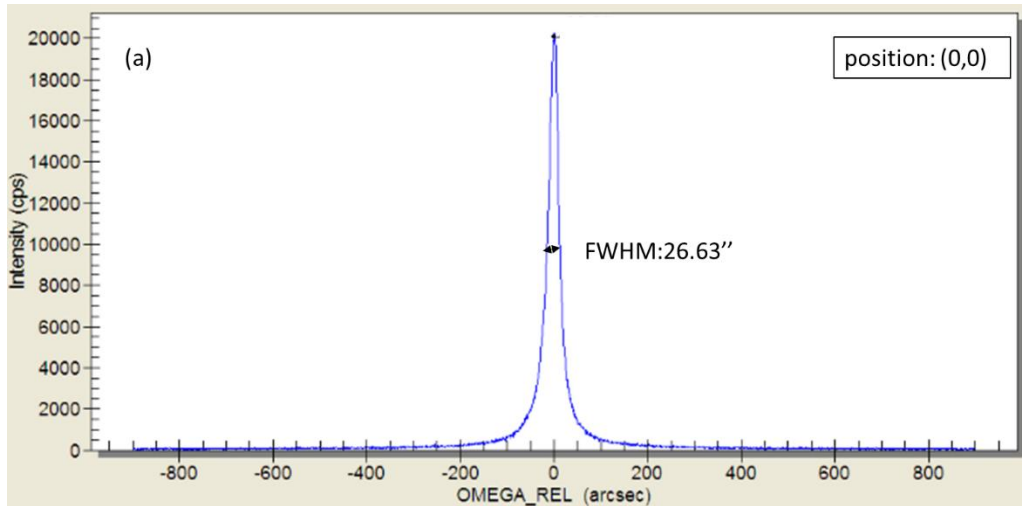
Fig 6.20 Omega Scan of Sample 7 in (a) (0,0) position; (b) (0,3) postion; (c) (0,-3) postion

Sample 8----Z4952

The picture of sample 8 is shown in Fig 6.21. The dimension of it is 10mm * 10mm. We did omega scan on three positions which are (0,0) (0,3) (0,-3) and the graph is shown in Fig 6.22.
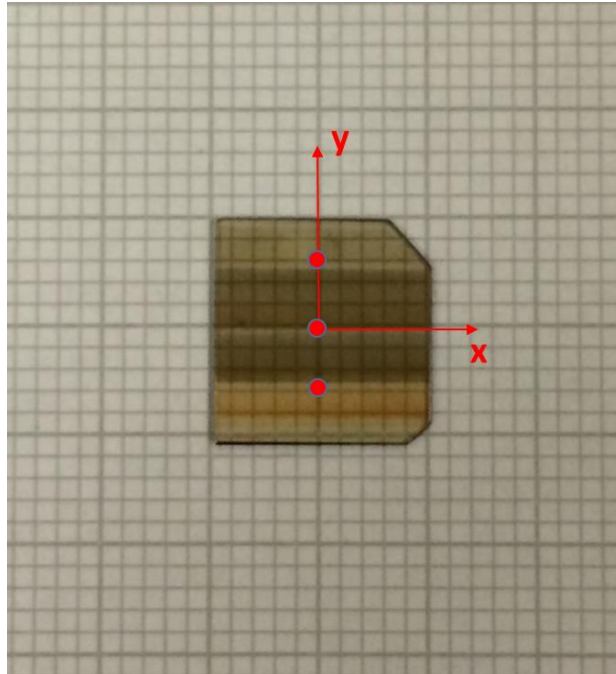
Fig 6.21 The picture of Sample 8 with three positions indicated by red dots
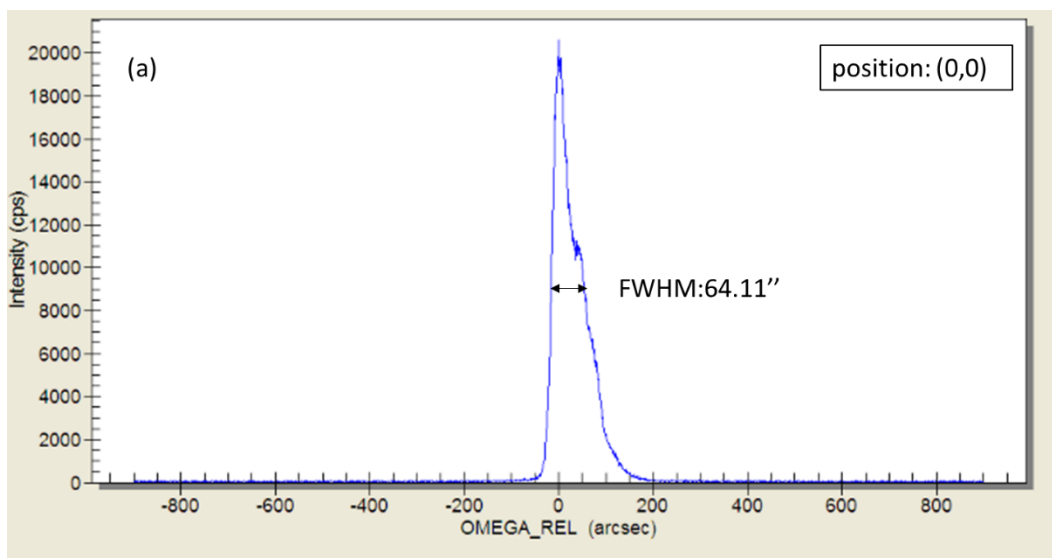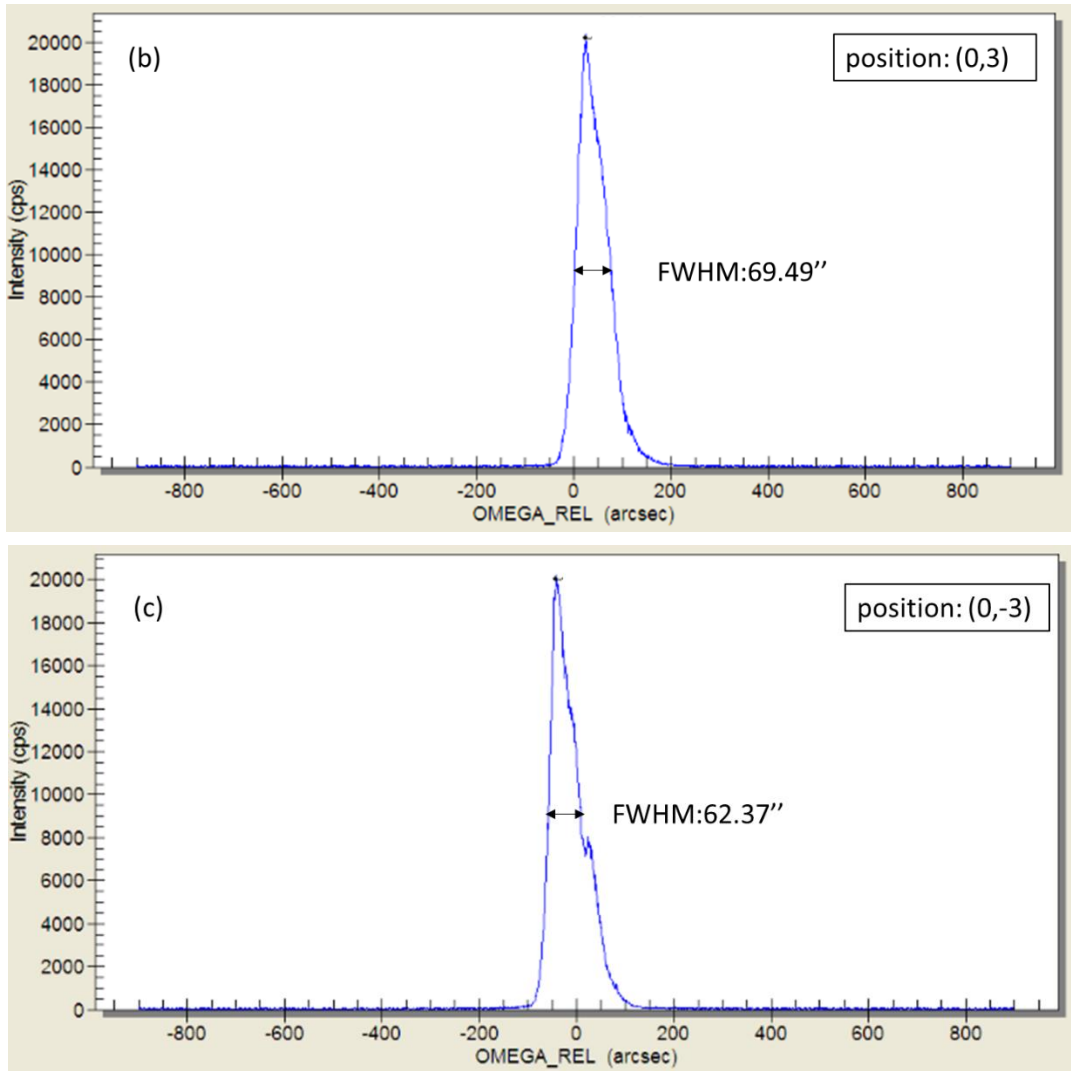
Fig 6.22 Omega Scan of Sample 8 in (a) (0,0) position; (b) (0,3) postion; (c) (0,-3) postion

The FWHM results of all 8 samples are summarized in the following table.

Table 6.1 FWHM results of all the samples

	FWHM at Position 1	FWHM at Position 2	FWHM at Position 3	Average FWHM	Ideal FWHM	Percentage Difference
Sample 1	27.94"	28.32"	29.11"	28.46"	24.10"	18.1%
Sample 2	31.29"	30.12"	34.32"	31.91"	24.10"	32.4%
Sample 3	41.38"	41.58"	38.76"	40.54"	24.10"	68.2%
Sample 4	58.33"	51.79"	84.29"	64.80"	24.10"	168.9%
Sample 5	58.37"	52.74"	55.34"	55.48"	26.30"	111.0%
Sample 6	90.68"	95.24"	90.03"	91.98"	26.30"	249.8%
Sample 7	26.63"	22.77"	45.91"	31.77"	10.40"	20.8%
Sample 8	64.11"	69.49"	62.37"	65.32"	10.40"	148.4%

The unit of FWHM is arc second and the percentage difference is defined as |average FWHM-Ideal FWHM|/Ideal FAHM x 100%

55

6.3 Conclusion

High Resolution X-ray Diffraction is used to measure the rocking curve of all the 8 samples, and Software HXRD is used to simulate the rocking curve for perfect crystal. Full Width Half Maximum is calculated to evaluate the overall quality of these 8 samples, and comparing them with perfect crystals. Since the FWHM stands for the overall quality of crystals, from table 6.1 we know the sequence of samples in a quality descending order is sample 1, sample 7, sample 2, sample 3, sample 5, sample 8 and sample 4.

Chapter 7. Summary

7.1 Conclusions

Defect characterization and analysis is done in Silicon Carbide substrate, homo-epilayer, and Gallium Nitride crystals. The combination of techniques such as Synchrotron White Beam X-ray Topography, Monochromatic X-ray, Nomarski Microscopy and High Resolution X-ray Diffraction are used. The density of Basal Plane Dislocation, Threading Edge Dislocation, Threading Screw Dislocation, and Full Width Half Maximum of the Rocking Curve are measured. Other defects like Stacking Fault, Micropipes and Low Angle Grain Boundary are characterized by SWBXT and V-shape inclusion is observed in Nomarski Microscope as well. Software LauPt is used to simulate the diffraction pattern in Synchrotron White Beam X-ray Topography, and Software HXRD is used to simulate the rocking curve in High Resolution X-ray Diffraction.

7.2 Future Work

For Silicon Carbide sample with homo-epilayer, in order to know more details about the V-shape defects, Scanning Electron Microscope can be used to observed the configuration of V-shape defects, and Raman Spectroscopy is expected to be used for detecting the chemical bond of this V-shape defect, determining the phase or structure of this inclusion. In regard to Gallium Nitride sample, SWBXT could be done on these sample to get better understanding of the defects structure in it.

Reference

[1] F. Wu, "Defect Characterization in 4H Silicon Carbide Bulk Crystals and Epilayers," 2014.

[2] M. Bhatnagar and B. J. Baliga, "Comparison of 6H-SiC, 3C-SiC, and Si for Power Devices," *IEEE Trans. Electron Devices*, vol. 40, no. 3, pp. 645–655, 1993.

[3] P. G. Neudeck, R. S. Okojie, and L. Y. Chen, "High-temperature electronics - A role for wide bandgap semiconductors?," *Proc. IEEE*, vol. 90, no. 6, pp. 1065–1076, 2002.

[4] Wikipedia, "Silicon." [Online]. Available: http://en.wikipedia.org/wiki/Silicon.

[5] Wikipedia, "Gallium Arsenide." [Online]. Available: http://en.wikipedia.org/wiki/Gallium_arsenide.

[6] B. J. Baliga, "Power Semiconductor Devices for Variable-Frequency Drives," *Proc. IEEE*, vol. 82, no. 8, pp. 1112–1122, 1994.

[7] B. J. Baliga, "Trends in power semiconductor devices," *IEEE Trans. Electron Devices*, vol. 43, no. 10, p. 1731, 1996.

[8] A. Elasser and T. P. Chow, "Silicon carbide benefits and advantages for power electronics circuits and systems," *Proceedings of the IEEE*, vol. 90, no. 6. pp. 969–986, 2002.

[9] C. E. Weitzel, J. W. Palmour, C. H. Carter, K. Moore, K. J. Nordquist, S. Alien, C. Thero, and M. Bhatnagar, "Silicon carbide high-power devices," *IEEE Trans. Electron Devices*, vol. 43, no. 10, pp. 1732–1741, 1996.

[10] R. J. Trew, "SiC and GaN transistors - Is there one winner for microwave power applications?," *Proc. IEEE*, vol. 90, no. 6, pp. 1032–1047, 2002.

[11] H. Wang, "Study of Growth Mechanism and Defect Origins in 4H-Silicon Carbide Substrate and Homoepitaxy," 2014.

[12] F. Wu, H. Wang, S. Byrappa, B. Raghothamachar, M. Dudley, G. Chung, D. Hansen, S. G. Mueller, and M. J. Loboda, "The Nucleation and Propagation of Threading Dislocations with c-component of Burgers Vector in PVT-Grown 4H-SiC," 2011, vol. 98, pp. 3–4.

[13] M. Dudley, Y. Chen, X. R. Huang, and R. H. Ma, "Aspects of Dislocation Behavior in SiC," *Mater. Sci. Forum*, vol. 600–603, pp. 261–266, 2009.

[14] P. G. Neudeck and A. J. Powell, "Performance limiting micropipe defects in silicon carbide wafers," *IEEE Electron Device Lett.*, vol. 15, no. 2, pp. 63–65, 1994.

[15] M. Dudley, X. R. Huang, W. Huang, a. Powell, S. Wang, P. Neudeck, and M. Skowronski, "The mechanism of micropipe nucleation at inclusions in silicon carbide," *Appl. Phys. Lett.*, vol. 75, no. 6, p. 784, 1999.

[16] W. Si, M. Dudley, H. Kong, J. Sumakeris, and C. Carter, "Investigations of 3C-SiC inclusions in 4H-SiC epilayers on 4H-SiC single crystal substrates," *J. Electron. Mater.*, vol. 26, no. 3, pp. 151–159, 1997.

[17] G. Kinetics, "Growth Kinetics and Thermal Stress in the Sublimation Growth of Silicon Carbide," *Cryst. Growth Des.*, vol. 2, no. 1, pp. 213–220, 2002.

[18] X. R. Huang, "LauPt." .

[19] F. Wu, S. Byrappa, H. Wang, Y. Chen, B. Raghothamachar, M. Dudley, E. K. Sanchez, G. Chung, D. Hansen, S. G. Mueller, and M. J. Loboda, "Simulation of Grazing-Incidence Synchrotron X-ray Topographic Images of Threading c+a Dislocations in 4H-SiC," in *MRS Proceedings*, 2012, vol. 1433, no. x, pp. mrss12–1433–h02–04.

[20] Y. Arroyo Rojas Dasilva, "Characterization of A-plane Grown GaN on Sapphire Substrates by Electron Microscopy," *Thesis*, 2009.

[21] Wikipedia, "Gallium Nitride." [Online]. Available: https://en.wikipedia.org/wiki/Gallium_nitride#Developments.

[22] "GaN Transistor." [Online]. Available: http://mitei.mit.edu/news/improving-transistor-small-device-big-energy-savings.

[23] X. R. Huang, "HXRD." .

[24] B. K. Tanner and D. K. Bowen, "Synchrotron X-radiation topography," *Materials Science Reports*, vol. 8, no. 8. pp. 371–407, 1992.